

Spherical body orientation extraction and Rayleigh-Bénard convection

M.W.M. Neut

May 1, 2014

UNIVERSITY OF TWENTE

MASTER THESIS

**Spherical body orientation
extraction and Rayleigh-Bénard
convection**

Author:
M.W.M. NEUT

Graduation committee:
E.P. VAN DER POEL, M. Sc.
Dr. ir. H.L. OFFERHAUS
Dr. C. SUN
Prof. dr. D. LOHSE

Summary

This thesis reports the work performed for obtaining a master's degree at the Twente University. It consists of two main parts. In the first part, a novel method for obtaining the absolute orientation of a spherical object is developed. The method is based on painting a specific pattern onto the surface of a sphere and minimizing a cost function based on the difference between a image recording of the physical sphere and a digital reference pattern. Contrary to existing methods that use brute-force comparisons and select the best fitting image from a reference database, the method introduced herein uses a minimization algorithm that does not require databases or calibration. Instead, it employs a specifically designed pattern that is painted on the surface of a sphere using a 3D-printed stencil, while the digital counterpart is a simple piece-wise constant boolean function. It is shown in chapter 3 that the resulting performance exceeds existing methods by at least one order of magnitude in both computation speed and accuracy and allows sub-degree real-time analysis of the absolute orientation of a sphere.

For the second part of this work, Rayleigh-Bénard (RB) convection is studied both experimentally and numerically. Experimentally, a quasi-two-dimensional RB convection setup is designed and built for both research and demonstrative purposes. As demonstration, shadowgraphy allows visualization of the complex dynamics of rising and falling thermal plumes inside a convection cell. The setup is proven very succesful in showcasing thermal convection with a table-top experiment. It is expected that the setup continues to be used for such demonstrations and provide insight into the field of fluid physics to the general public. In addition to Rayleigh-

Bénard experiments, the setup can be used for boiling experiments with only minor modifications.

Also, a relatively novel technique called background-oriented schlieren [17] is elaborated and applied to the setup. This method allows resolving the temperature field of the thermal convection cell. The temperature field can be used for statistical analysis on the dynamics of the system. We hypothesized that with the conservation laws that govern these dynamics, the velocity field can be resolved from the temperature field (if known with sufficient spatial and temporal resolution). Unfortunately, however, we prove in section 6.5 that it is mathematically impossible to uniquely recover the velocity field from the temperature field.

Finally, a novel direct numerical simulation code is used to study the influence of strong geometric confinement on heat transport in RB convection. It was recently shown [16] that heat transport enhancement is observed for moderate confinement, despite an overall decrease in flow velocity due to increased viscous drag from the sidewalls. In this thesis, we study a larger range of aspect ratios and show that heat transport does increase for moderate confinement, but peaks and decreases for very strong confinement. In addition, the code is used for design of the experimental setup.

Contents

I	A method for obtaining the orientation of a spherical body from visual observation	9
1	Introduction	11
1.1	Particles in turbulence	11
1.2	Existing techniques	13
2	Method	15
2.1	Overview	15
2.2	Pattern projection	17
2.3	Rotation	18
2.4	Painting stencil	20
2.5	Minimization	21
2.5.1	Objective	21
2.5.2	Nelder-Mead	22
2.5.3	Pattern	23
2.6	Accuracy	25
2.6.1	Experimental accuracy	26
2.6.2	Numerical accuracy	27
2.7	Performance	29
3	Results	31
3.1	Painting stencil	31
3.2	Accuracy	33
3.2.1	Experimental accuracy	33
3.2.2	Numerical accuracy	35
3.3	Performance	37

4	Concluding remarks & recommendations	39
4.1	Conclusions	39
4.2	Recommendations	40
II	Rayleigh-Bénard convection	43
5	Introduction	45
5.1	Natural convection	45
5.2	The Boussinesq approximation	46
5.3	Rayleigh-Bénard convection	50
5.4	Experimental methods	52
5.5	Numerical methods	53
6	Thin-cell Rayleigh-Bénard convection setup	55
6.1	Introduction	55
6.2	Experimental setup	56
6.2.1	Design	56
6.3	Visualization methods	61
6.3.1	Theory	61
6.3.2	Shadowgraph imaging	64
6.3.3	Background-oriented schlieren	66
6.4	Results	69
6.4.1	Experimental setup	69
6.4.2	Shadowgraphy visualization	71
6.4.3	Background-oriented schlieren	72
6.5	Derivation of velocity quantities	75
6.5.1	Hypothesis	75
6.5.2	Proof	77
6.6	Conclusions & recommendations	81
7	Spatially confined thermal convection cells	83
7.1	Introduction	83
7.2	Background & method	84
7.3	Results	85
7.4	Conclusions & recommendations	87
	Acknowledgements	89

References	92
Appendices	95
A Sphere pattern in FORTRAN syntax	97
B Non-dimensionalization of Boussinesq approximation	99

Part I

A method for obtaining the orientation of a spherical body from visual observation

Chapter 1

Introduction

1.1 Particles in turbulence

Freely advected rigid particles suspended in a fluid flow are subject to both translational and rotational degrees of freedom. The dynamics of such particles strongly depend on their size and the viscosity of the surrounding fluid. These properties are combined into a dimensionless number known as the Stokes number, defined as

$$\text{St} = \frac{\tau U}{D} \quad (1.1)$$

where τ is the particles relaxation time (the time constant in exponential velocity decay due to drag), U is the fluid velocity far away from the particle and D is the characteristic dimension of the particle (typically its diameter). Particles with low St are advected by the flow and follow the fluid streamlines, which is the case for particles where its typical dimension is smaller than the smallest scales of the flow, the Kolmogorov scale η . Due to its size, the flow around a particle is locally laminar and the physics can be described as *Stokes flow*. In the limit where $D \rightarrow 0$, the velocity of a neutrally buoyant particle reduces to the surrounding fluid velocity and the rotation and translation are effectively decoupled [8]. This

property is crucial in *particle tracking velocimetry* (PTV) where small tracer particles are seeded to a flow. As the particles follow the fluid streamlines, their trajectories enable flow visualization.

As illustrated in figure 1.1, the dynamics of particles with typical dimension larger than η are much more complex than those of tracer particles. It is clear that for these scales, rotation and translation are interconnected as the rotation-induced Magnus force directly affects the particle's trajectory.

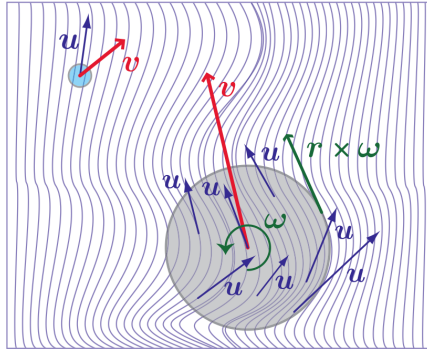


Figure 1.1: Illustration of the body forces that act upon small and large objects in a flow. The flow around the small particle is smooth and the particle acts as a tracer, whereas the flow around the large particle exhibits significant spatial variations. Illustration courtesy of [8].

To study the physics of these larger particles, it is crucial to obtain reliable experimental data. The use of video footage for analysis is preferred and commonly used in the fluid community due to its non-invasiveness and straightforward implementation. Determining the translation from video footage has been studied thoroughly and is even commercially exploited in many forms like ball-tracking in sports. Rotation, however, has only recently been subjected to study.

The objective of this field of study is to resolve and understand the six degrees of freedom of the particle dynamics, i.e. to track both the translation and rotation of large particles in turbulence. Recent studies have shown interesting intermittent behavior in the particles rotation, and while it is expected that this is caused by the complex interaction between the particle and its wake, the exact mechanism is still unknown. In addition, studies

of human motion for rehabilitation purposes or athletic performance rely on robust tracking systems and similar systems are used in the gaming industry to create more natural movements in video games. Most of these systems only capture translation and retrieve orientation from the relative motion of translating vertices.

Part II of this thesis provides a novel technique that is both faster and more accurate than existing techniques in determining the absolute orientation of a spherical body. Like any such improvement, it enables a more reliable and accurate understanding of the underlying physics.

This work is currently under evaluation for publication as *Method and experimental results for obtaining the absolute orientation of a spherical body using recorded footage* in the European Journal of Mechanics – B/Fluids.

1.2 Existing techniques

Several previous studies focused on the measurement of the angular velocity without resolving the absolute orientation as function of time. One technique involves drawing dots on the surface of a sphere and tracking these dots using a high-speed camera system [9]. Another method [10] involves specifically engineered transparent particles with an embedded mirror. Measurements of the times required for laser reflections from the mirrors to rotate through the small angle defined by a pair of slits then yields the rotation rate. Unfortunately, this technique only allows for a single rotation parameter to be measured.

Exponentially growing computing power has allowed for more advanced optical techniques to become increasingly sensible. The present state-of-the-art method for resolving the absolute orientation is based on a pattern-matching algorithm we refer to as Zimmerman's method [7]. It consists of drawing a uecific pattern onto the surface of a sphere and subsequently creating a database of 2D projections for the entire range of orientations. A database with limited resolution is created for each sphere individually by taking pictures from various angles. These pictures are provided to a MATLAB toolbox which subsequently generates millions of 2D projections from the input pictures.

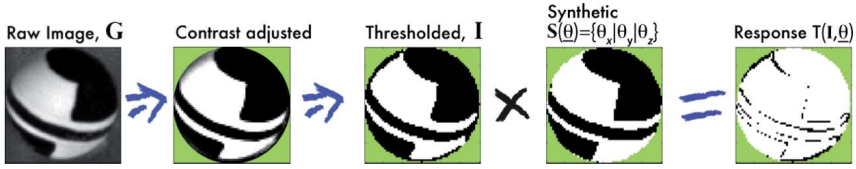


Figure 1.2: Flow process of Zimmerman's method. Recorded footage is contrast-adjusted and thresholded, and subsequently compared to a large set of images of known orientations. The response indicates the match between the measurement and database reference.

Resolving the actual orientation consists of comparing the measured image to the database. This process is illustrated in figure 1.2. The step called *Response* is formed by multiplication of a given measured image and the corresponding synthetic image, where the synthetic image is obtained from the database created earlier. Using a brute-force method, several initial coarse candidate orientations are selected from the database. A local refinement is applied around these candidate orientations and the locally refined candidate that best matches the measured image is selected. This process is repeated for each movie frame of a recording. Finally, a graph of possible candidates is generated, and a Dijkstra shortest-path-finding algorithm is used to find the most likely absolute orientation over time, omitting false data points and interpolating where necessary.

Although theoretically advanced, Zimmerman's method has some practical disadvantages. Foremost, each sphere requires a new database, which creation is a rather cumbersome and fallible process as it involves photographing each painted sphere from six specific angles prior to experimenting. This database also directly restricts both the accuracy and performance of the method. In addition, the requirement of an optimizing post-processing step indicates an inherent shortcoming of the candidate database method.

Chapter 2

Method

2.1 Overview

The method proposed in this report employs a very different approach than Zimmerman's method. It is a method that does not require any pre- or post-processing, vastly reducing complexity while increasing accuracy and performance.

In essence, the method can be divided into four parts. Initially, a suitable boolean pattern is created. This pattern can be described as a piecewise constant function such that, given a coordinate on the surface of a sphere, the function returns either zero or one depending on the color of its corresponding infinitesimally small surface element. It is important that this pattern is defined for the full range of spherical coordinates with fixed radius (i.e. the entire surface of the sphere). Second, the pattern is drawn onto an identical physical sphere. This is realized using a 3D-printed painting stencil and an airbrush system. The exact pattern is elaborated in section 2.5.3.

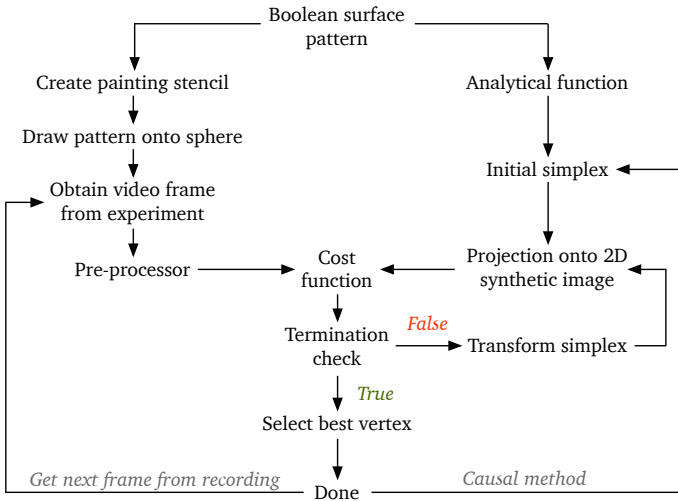


Figure 2.1: Flowchart illustrating a schematic overview of the method. Starting with the boolean surface pattern, a physical sphere is created which is subsequently compared to an analytical function in experiments to determine the absolute orientation. After each frame, the initial estimate for the next frame is passed on to the algorithm to reduce the computation time. The *initial simplex* is a geometrical shape that is used in the minimization algorithm and is elaborated in section 2.5.

Third, a synthetic 2D image is constructed from a projection of the surface of the sphere onto a plane. This projection is a function of the angles of rotation of the sphere, meaning a synthetic image can be generated for every possible orientation. As the pattern is defined for a continuous range of the sphere's surface, there is no limit to the projection's resolution.

Finally, the rotated and projected synthetic pattern is compared to an image of the physical sphere. The difference between these images is reduced to a scalar value using a cost function. The arguments for which this cost function has a global minimum then determines the absolute orientation, and the specific pattern in combination with a simplex-based minimization algorithm enables the global minimum to be found very efficiently. The general process is shown schematically in a flowchart in figure 2.1 and the simplex-based minimization algorithm is elaborated in section 2.5.

2.2 Pattern projection

The surface of a unit sphere¹ can be described in spherical coordinates as the two-dimensional span of the azimuthal and polar angle (θ and ϕ , respectively). We introduce a piece-wise constant boolean function $F(\theta, \phi)$ that describes the pattern exactly for any coordinate on the spheres surface (returning a zero or one). Plotting this function with unit radius and using yellow and black to represent the different boolean output of the function yields an illustration as shown in figure 2.2. The exact pattern is described in paragraph 2.5.3.

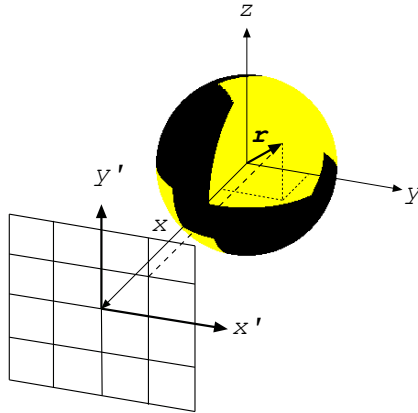


Figure 2.2: Projection of the surface of the pattern onto a 2D grid. A line parallel to the x -axis is drawn towards the surface of the sphere from each gridpoint. The coordinates \mathbf{r} of the intersection are calculated using eqs. (2.1)–(2.5).

As stated in the overview, the cost function is calculated from some measured image and a synthetic projection image. The latter is generated by introducing a plane of two by two units with its center at $\frac{x}{R} > 1$ and its normal directed towards the origin. This plane is then divided into a (N by N) grid, and a line is drawn parallel to the x -axis towards the negative x -direction for each of the gridpoints. The spherical coordinates at which

¹A sphere with radius $R = 1$ (dimensionless units).

this line intersects with the sphere surface can be geometrically derived and are given by:

$$\phi = \text{acos} \left(y'_j \right), \quad (2.1)$$

$$\theta = \text{asin} \left(\frac{x'_i}{\sin \phi} \right). \quad (2.2)$$

Here, the accents denote the projection plane axes and i and j represent the grid points as shown in figure 2.2. The resulting image is a (parallel) projection of the sphere's surface. Note that the resolution can be set to any preferred value as it is only determined by the gridsize N . This allows matching the synthetic image size to the measured image size (in pixels), which is required to calculate the cost function.

2.3 Rotation

Section 2.2 describes the projection of the spheres surface onto a 2D grid called the synthetic image. However, this projection must be orientation-dependent which is realized by rotating the sphere itself prior to projecting it onto the grid. Therefore, we require the Cartesian coordinates of the surface elements corresponding to each of the gridpoints in the projection grid. Since the radius of the sphere is 1, we calculate its coordinates $\mathbf{r} = (x, y, z)$ using:

$$x = \sin(\phi) \cos(\theta), \quad (2.3)$$

$$y = \sin(\phi) \sin(\theta), \quad (2.4)$$

$$z = \cos(\phi). \quad (2.5)$$

Next, we rotate each of the Cartesian coordinates around the origin. There is no scientific consensus on the best method of rotating, though a common method is the use of a rotation matrix in combination with some definition of Euler angles. Unfortunately, Euler angles are prone to a problem called *gimbal lock*, in which case the axes of two of the three gimbals are prompted

into a parallel configuration, leading to the loss of one degree of freedom. Though technically the gimbals are not locked, it leads to a degenerate case where it is impossible to trace back the absolute orientation of all three gimbals.

The use of a fourth axis, quaternions or the axis-angle convention resolves this problem. We use the *axis-angle* convention considering its comprehensible, singularity-free definition and straightforward implementation at the cost of a minor performance decrease.

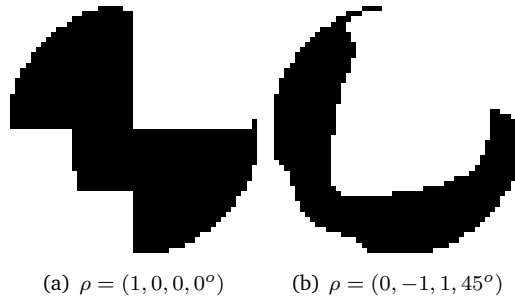


Figure 2.3: Projection examples of synthetic image $S = S(\rho)$ for various rotation parameters ρ and gridsize $N = 50$.

The rotation of a vector in three dimensions is realized using a rotation matrix or using Rodrigues' formula:

$$\tilde{\mathbf{r}} = \mathbf{r} \cos \alpha + (\mathbf{k} \times \mathbf{r}) \sin \alpha + \mathbf{k} (\mathbf{k} \cdot \mathbf{r}) (1 - \cos \alpha). \quad (2.6)$$

Here, \mathbf{r} and $\tilde{\mathbf{r}}$ are vectors (in Cartesian coordinates) before and after rotation. The vector \mathbf{k} and angle α are the axis and angle of rotation. After applying a rotation, the *rotated* azimuth and polar angles can be retrieved using $\tilde{\mathbf{r}}$ and the inverse of eqs. (2.3)–(2.5). Next, the pattern function F is called at the *rotated* azimuth and polar angles. Combined with the projection, an N by N synthetic image S can now be generated using the rotation parameters \mathbf{k} and α . These four parameters are combined into one vector as $(k_x, k_y, k_z, \alpha) = \rho$. A sample output is shown in figure 2.3.

2.4 Painting stencil

Calibration is of crucial importance in absolute measurements. Often, this is solved by zeroing the apparatus in question. However, a causality problem arises which rules out this possibility as there is no absolute zero in this problem. Zimmerman's method tries to mitigate this by mapping each sphere individually, making reference pictures from several angles. However, these pictures have to be taken at known angle which is unfortunately sensitive to human error as the sphere itself must be re-positioned in-between pictures.

Our method assumes the synthetic projection as absolute reference, and we dismiss many sources of error by introducing a painting stencil that acts as a scaffold for painting the pattern onto a spheres surface.

The painting stencil consists of two 3D-printed halves, together referred to as the *shell*. The shell is designed such that it forms a painting template for an encapsulated sphere. The covered parts of the sphere are not affected when spray-painting a (blank) sphere inside the shell, leaving an exact physical representation of the pattern on the surface of the sphere. The obvious advantage of this method is that it allows for high repeatability without the need for mapping each individual sphere prior to experimenting. A rendering of the stencil is shown in figure 2.4.

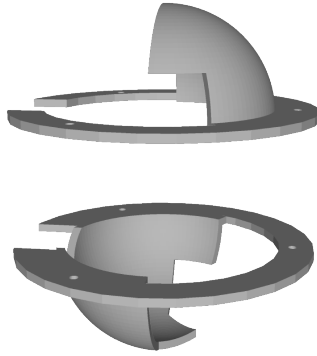


Figure 2.4: Computer generated rendering of the painting stencil. The two halves are aligned using the mounting holes in the rim.

The process of painting starts with placing a blank sphere inside one half of the shell. Next, the other half is placed on top such that the holes in the encompassed rings match. Screws subsequently keep the shells halves aligned while a small diameter difference of the shell and sphere secures the encased sphere against rotating inside the shell. Note that each sphere size requires its own stencil, and stencils can easily be re-used.

2.5 Minimization

2.5.1 Objective

We define a cost function

$$\mu(\rho) = \sum |\mathbf{S}(\rho) - \mathbf{M}| \quad (2.7)$$

where \mathbf{M} is some measured image or movie frame, \mathbf{S} is the synthetic image and Σ indicates a summation over each grid-point of the images. As stated in section 2.1, minimization of this cost function yields the best match between \mathbf{M} and \mathbf{S} which means the objective is to solve **argmin** $\mu(\rho)$. In

other words: to find ρ such that μ is minimized (globally). Also note that \mathbf{M} and \mathbf{S} must be of equal dimensions and that the pattern must be unique for every orientation. The latter is elaborated in paragraph 2.5.3.

2.5.2 Nelder-Mead

There are several methods to solve such minimization problems. We use the Nelder-Mead method (NMM) for its multidimensionality, unboundedness and clear implementation. It is a heuristic simplex search algorithm and is one of the most used minimization algorithms and is specifically suitable for solving parameter estimations of discontinuous or discrete functions like our cost function (2.7) as it does not require derivatives. It is based on the transformation of a geometric shape around a local minimum within the parameter space. The geometric shape, a simplex \mathbb{R}^k -space is defined as the convex hull of any affinely independent² set of $k + 1$ points. For example, a simplex in two dimensions is a triangle and a tetrahedron in three dimensions.

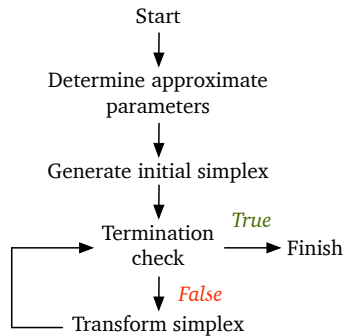


Figure 2.5: Flowchart illustrating the schematic process of the Nelder-Mead method. Starting with an approximate solution, an initial simplex is generated, which is transformed such that its vertices advance towards a local minimum until a termination criterium is met. The best vertex subsequently corresponds to the local minimum.

The method is quite simple, and the main process is illustrated in figure 2.5. The process starts with *Determine approximate parameters*, in which an

²all lines between all points are linearly independent

initial estimate of the parameters is provided to the algorithm. This estimate is used as a basis for the *Initial simplex generation*, where a simplex around the initial estimate is created. The size of the simplex must be related to the expected size of the parameter space in which a minimum should be found, or sometimes the simplex' vertices are directly defined. Next, the algorithm performs several termination checks. The process terminates if (1) the vertices are adjacent within some threshold, (2) the function values themselves are sufficiently close or (3) a failure to converge termination, when a preset maximum number of iterations is reached.

If the termination check returns false, the algorithm transforms the current simplex. The transformation deforms the simplex such that its vertices advance towards the local minimum and consist of three steps:

- I **Ordering:** Determine the indices of the worst, second worst and best vertex.
- II **Centroid:** Compute the centroid of the best edge. This is the edge opposite of the best vertex.
- III **Transform:** Compute the new simplex from the current one. First, try to replace the worst vertex by *reflection*, *expansion*, *contraction* with respect to the best side. If the new vertex is accepted, it becomes the new vertex of the simplex. Otherwise, *shrink* the simplex towards the best vertex.

The simplex transformations are relatively straightforward and follows after sorting the indices h , s and l of the *worst*, *second worst* and *best* vertex (the ranking is based on the cost function). More details on the transformations can be found in [4] and [11].

2.5.3 Pattern

The iterative nature of the NMM is sometimes considered unwanted when exact solutions are required, but it is actually advantageous when used with a suitable pattern, as the pattern itself leads the NMM to the global minimum. The requires the pattern to be constructed such that there exists a curve $\eta(t_i)$ in the solution space ρ that connects the initial estimate to the global minimum for which

$$\frac{\partial \mu}{\partial \eta} < 0 \quad \forall t_i \tag{2.8}$$

Here, t_i is the position on this curve at iteration i . This means that an iteration in the right direction (towards the minimum) directly yields the cost function to return a lower value and vice versa. Consequently, the pattern must consist of a single continuous patch of black or white.

In addition, uniqueness of the pattern within the solution space is crucial for correct operation of the algorithm. We therefore add small features to distinguish possible ambiguities. These features expand or contract the continuous patch locally such that the pattern remains one simply connected region of black or white.

It is convenient to depict a cube around the sphere, such that we can refer to its six sides. Using this definition, the pattern looks as shown in figure 2.6. An exact description of the function (θ, ϕ) that describes this pattern can be found in Appendix A.

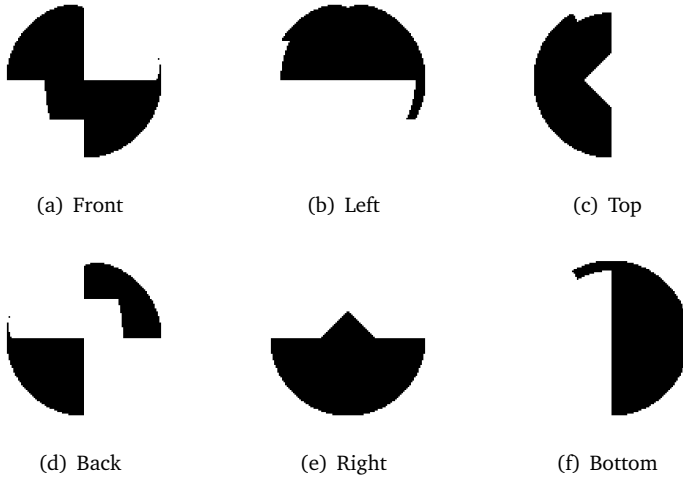


Figure 2.6: Several viewpoints of the pattern. Here, the synthetic projection is defined in the axis-angle convention as front: $\rho = (1, 0, 0, 0^\circ)$, left: $\rho = (0, 0, 1, -90^\circ)$, top: $\rho = (0, 1, 0, -90^\circ)$, back: $\rho = (0, 0, 1, 180^\circ)$, right: $\rho = (0, 0, 1, 90^\circ)$ and bottom: $\rho = (0, 1, 0, 90^\circ)$.

2.6 Accuracy

We define the accuracy of our method as the standard deviation of the difference between a reference orientation and the orientation as solved by our method. Unfortunately, direct measurement of the experimental error is not possible as the exact reference orientation is not known. Therefore, an indirect measurement is used to determine the *experimental accuracy*. In addition, we define a *numerical accuracy* which is determined by generating a synthetic image with known orientation and resolving the orientation of this generated image using our method.

Also, although the axis-angle convention is straightforward to implement into an algorithm, its quantities are not very intuitive. Therefore, we perform a coordinate transform of the resolved orientations from axis-angle

to XYZ-Euler (fixed axes) convention. We define this transformation as:

$$\epsilon = f(\rho) \quad (2.9)$$

where

$$\begin{pmatrix} \epsilon_x \\ \epsilon_y \\ \epsilon_z \end{pmatrix} = \begin{pmatrix} \text{atan2} \left(k_y \sin \alpha - k_x k_z (1 - \cos \alpha), 1 - (k_y^2 + k_z^2) (1 - \cos \alpha) \right) \\ \text{asin} (k_x k_z (1 - \cos \alpha + k_z \sin \alpha)) \\ \text{atan2} (k_x \sin \alpha - k_y k_z (1 - \cos \alpha), 1 - (k_x^2 + k_z^2) (1 - \cos \alpha)) \end{pmatrix} \quad (2.10)$$

Here, $\epsilon = (\epsilon_x, \epsilon_y, \epsilon_z)$ describes the transformed resolved orientation. The XYZ-Euler convention enables expressing the error in degree angle, which is a relatively intuitive way of characterizing accuracy.

Finally, as we describe the experimental and numerical error in a scalar value σ_e and σ_n which are defined as the standard deviations of the differences or residual between the reference and measured (using our method) orientations.

$$\sigma = \text{std} |\epsilon_{\text{R(eference)}} - \epsilon_{\text{M(easured)}}| \quad (2.11)$$

2.6.1 Experimental accuracy

The experimental accuracy is verified indirectly using recorded footage of rising buoyant spheres. The required pattern is painted onto the surface of the spheres and the spheres are released separately from the lower part of the transparent section of the Twente Water Tunnel facility (TWT), which is shown schematically in figure 2.7. The TWT is an 8 meter high facility in which strong turbulence can be created using an active grid. This setup is used to study light (buoyant) particles in turbulence [5] and can also easily be utilized for validation of our algorithm. In our setup, spheres are released separately from the lower part of the transparent section of the TWT using a release mechanism and the buoyancy driven motion of a rising



Figure 2.7: Twente Water Tunnel facility

sphere is recorded using a high speed camera. Next, the recordings are cropped around the region of interest using a circular Hough transform and are contrast-adjusted and re-sized to form images similar to the synthetic images in size and shape. The resulting images are provided to the algorithm and subsequently solved for their orientation. If desired, a synthetic projection of the resolved orientation can be generated. This process is shown in figure 2.8.

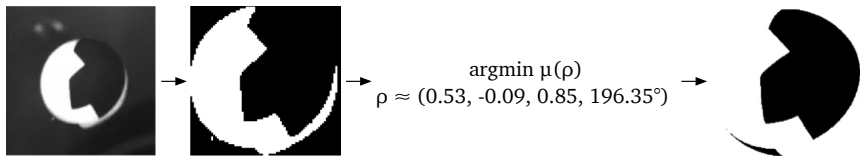


Figure 2.8: Several steps in the process of resolving the orientation. Initially, a sphere is placed inside the TWT and footage is recorded. The first image shows a loosely cropped snapshot of an example recording. The next image shows the contrast-adjusted and tightly cropped black-and-white image of the recording. This image is used as input for the algorithm, which finds the absolute orientation. The last image shows a synthetic projection of the corresponding orientation which clearly matches the original footage.

Repeating this process for each frame of a recording yields a data-set of resolved orientations and corresponding synthetic projections. As there is no absolute reference, we use the smoothness of the orientation in time. In addition, we assume that the rotation between two movie frames of that recording is small (up to approximately 10 degrees). The buoyancy-driven motion of a sphere in a stagnant flow can be considered smooth and continuous [7] and given a sufficiently small window of time, the rotational motion only exhibits smooth, low-frequency features. Hence, we attribute high-frequency motion to error of the measurement and approximate the actual motion by piece-wise fitting cubic polynomials to the data and consider the best fit of the data set as the reference orientation.

2.6.2 Numerical accuracy

The theoretical verification of our method uses computer-generated images of the sphere, similar to those shown in figure 2.6. These images provide a

perfect representation of their corresponding orientations, such that a set of perfect images with known reference orientation is created.

This set of computer-generated or *synthetic* images is resolved by our method and the results are compared to the synthetic reference orientation. Although the numerical error should theoretically be zero, this only holds for infinite resolution ($N \rightarrow \infty$). The reason for this is that the NMM minimizes a discrete cost function using floating point parameters (ρ) which implies there is a finite range in the parameter space that yields the same cost function output. The size of this range is directly related to the resolution N and determines the numerical and theoretical maximum accuracy for that resolution.

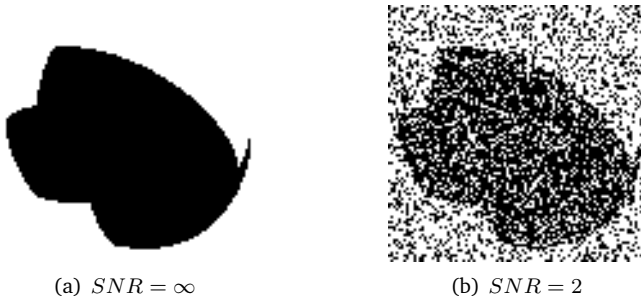


Figure 2.9: Example of the effect of salt & pepper noise for a signal-to-noise ratio (SNR) of ∞ (undistorted, left) and 2 (right). It can be seen this type of distortion does not significantly affect the image as one can still recognize the orientation by naked eye.

An indication of robustness is given by addition of *salt & pepper noise*³ to the generated images prior to resolving their orientation. Analogous to the ideal numerical error, this noisy numerical error is directly related to the resolution and signal-to-noise ratio.

³Randomly occurring black and white pixels

2.7 Performance

The performance of our method is determined mostly by the efficiency of computation and the desired accuracy. The most important factor in efficiency is the the degree of parallelization of computation, and the accuracy is mostly determined by the resolution N . Parallel computation can be applied to this algorithm. A crucial condition for parallelization is that certain computational steps are independent, which is the case for most image editing processes. In the case of our method, the computation of the cost function (eq. (2.7)) and the projection (such as in figure 2.3) are independent for each pixel of the image, and can be computed in parallel.

For parallel scaling studies, we use the *OpenMP* API which allows shared memory multiprocessing and can easily be implemented into our code. For practical purposes, the strong scaling of the code is studied. Strong scaling is defined as how the total computation time depends on the number of threads (processors) for a fixed problem size; i.e. the speedup as a function of the number of processors, with respect to the case of a single thread.

Although the NMM is guided towards the global minimum by the pattern in most cases, local minima may still occur. This can be solved by exhaustive scanning of the parameter space for each frame and choosing the lowest local minimum as the global minimum. This is done by restarting the algorithm at 208 initial conditions (26 axes at 8 angles) ⁴. We refer to this mode as *blank* solving and is very time-consuming. Fortunately, this mode is only required once when using what we call the *causal* method. In this method, the NMM assumes an educated guess near the global minimum. In practice, this educated guess is drawn from the solved orientation of the previous movie frame. The result is that the number of iterations of the NMM is reduced drastically when analyzing movies.

⁴This number may be greatly reduced, see section 4.2.

Chapter 3

Results

3.1 Painting stencil

Several iterations of patterns and production methods were evaluated. Due to the advantages of rapid prototyping that 3D-printing offers, it was decided to use a form of 3D printing to create the stencil. Initially, stencils were printed using an extrusion deposition method called fused deposition modeling (FDM). It was found that this method is not sufficiently accurate to allow for spray painting as the surface finish of the material leaves the extrusion profiles exposed. This is shown schematically in figure 3.1b. The effect of this surface finish is that sphere will not be encapsulated seamlessly which causes paint leakages and therefore an erroneous profile on the surface of the sphere.

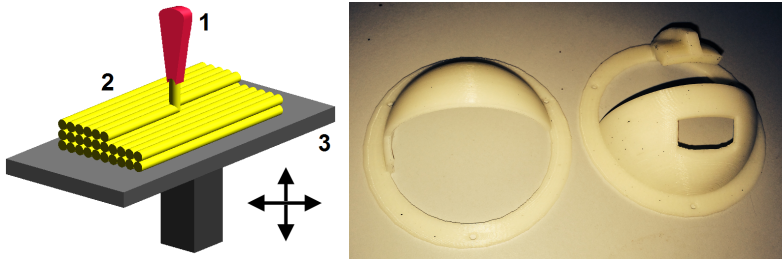


Figure 3.1: Schematic process (left, courtesy of Wikipedia) and example product (right) of a 3D-printing technique called fused deposition modeling (FDM). Note that the extrusion profiles remain visible on the surface of the finished product.

Selective laser sintering (SLS) is another 3D-fabrication method that allows for higher resolution fabrication, without leaving extrusion marks. The printed stencils are also easily polished to a smooth surface finish, allowing for a seamless interface between the stencil and the encapsulated sphere. It was found that stencils printed using the SLS method (and subsequently polished) meet the requirements for a painting stencil.



Figure 3.2: A finished painting stencil after several uses (left) and an example sphere as spray-painted using the stencil (right).

Application of paint using the stencil was done using a standard airbrush apparatus. A sample result is shown in figure 3.2b. It can be seen that the

edges show a sharp contrast between the light and dark sections of the profile.

In addition, the NMM requirement of a single large patch of black or white is also beneficial to the painting stencil as it can consist of a continuous covering structure. In contrast, having islands of patches occur in the pattern would require overhang bridges in the stencil which add complexity and difficulty in painting.

3.2 Accuracy

3.2.1 Experimental accuracy

The experimental error is determined from recordings at 1000 frames per second (fps) of buoyancy-driven rising spheres inside the TWT. The recordings are cropped around the sphere and re-sized¹ to a resolution of $N = 80$ to remove interframe size variations that may arise after automated cropping. It was found that recording at 1000 fps was sufficient to visualize the buoyance driven motion of rising spheres, as the the rotation between two frames is very small (several degrees at most). Therefore, the causal solving mode is applied to all physical experiments, and no post-processing is applied. The results of a typical measurement recording is shown in figure 3.3a. For this set, the data is piece-wise (in two segments) fitted using a cubic polynomial function and the residuals are shown in figure 3.3b. It can be seen that the output of the algorithm shows little deviation from smooth and continuous motion, which is confirmed by the residual plot.

¹In the original footage, the spheres are approximately 90 pixels in diameter.

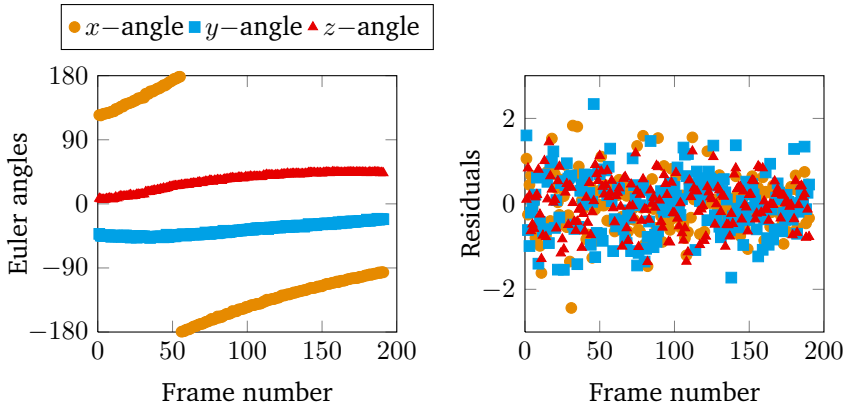


Figure 3.3: The left graph shows an example measurement as recorded in the TWT. The data is piece-wise (in 2 segments) fitted using a cubic polynomial function which is not plotted for clarity. Instead, the residuals are shown in the right plot.

In figure 3.4, several example results are shown. The top row are cropped sections of the raw high-speed footage. The bottom row are synthetic projections of the corresponding orientations as solved by our algorithm, visually confirming that our method solves the correct orientation.

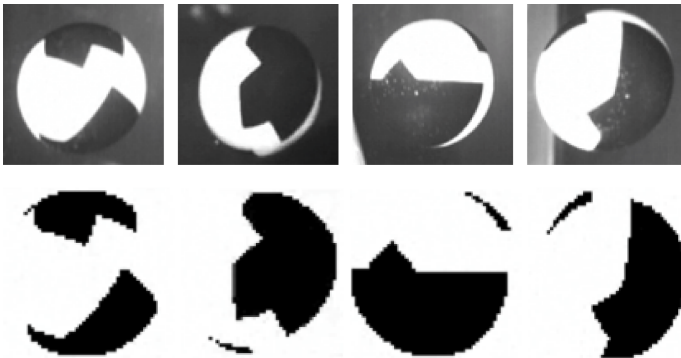


Figure 3.4: Example results of recorded images. The top row are loosely cropped snapshots of recorded footage and the bottom row are synthetic projections of the orientation as solved by our method. A good visual correspondence can be seen between the two images.

The probability density function (PDF) of this example is shown as the dotted line in figure 3.5 as the dotted line. The solid line represents the same sample data, but cropped to $N = 50$ prior to resolving their orientations, displaying the effect of resolution on accuracy. The standard deviation of the solid blue line is approximately 0.7 degrees and 1.2 degrees for the dashed red line. The effect of resolution on accuracy is elaborated on in section 3.2.2.

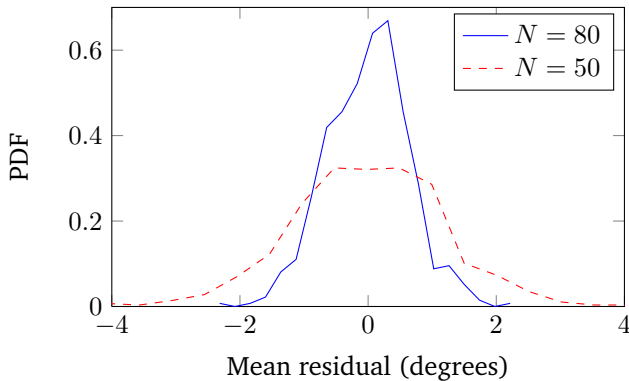


Figure 3.5: Plot of the probability density function of the mean residual of the example dataset of figure 3.3. The standard deviation for $N = 50$ is 1.2 degrees and 0.7 degrees for $N = 80$, demonstrating sub-degree accuracy.

The original recording of the example and other datasets with inlay of a synthetic projection can be found in supplemental material.

3.2.2 Numerical accuracy

Using the synthetic projections of several sets of 1024 randomly generated orientations, the numerical error as a function of image size (resolution) N is determined. The PDF of the numerical error is shown in figure 3.6. Note that the numerical error only depicts the approximate size of the parameter space that yields the same cost function for various resolutions, as explained in section 2.6.2.

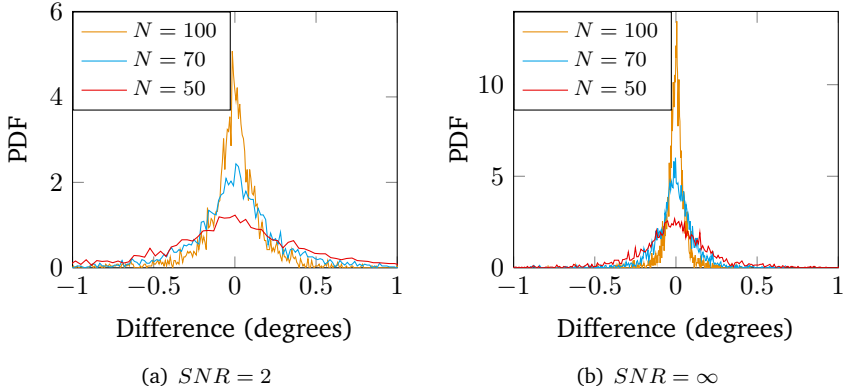


Figure 3.6: Numerical accuracy of our method for various resolutions N and SNR . It can be seen that the distributions resemble a normal distribution. In this example, the standard deviation is 0.75 degrees for $N = 50$ and $SNR = 2$ and 0.06 degrees for $N = 100$ and $SNR = \infty$, demonstrating sub-degree accuracy.

It can be seen that the accuracy of our method increases significantly with the resolution N ; the standard deviation decreases from 0.27 to 0.06 degree angle for the perfect image and decreases from 0.75 to 0.21 for the distorted image (for $N = 50$ to $N = 100$, respectively).

To determine the scaling of the numerical error, the standard deviation of error as a function of the resolution N is determined for $N = 50$ to $N = 100$. A set of 1024 synthetic orientations are created for each value of N and subsequently solved using our method. The results are shown in figure 3.7.

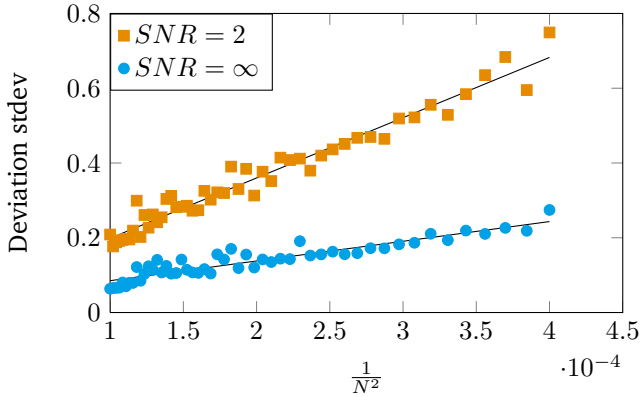


Figure 3.7: Scaling of the standard deviation of the numerical error as function of the resolution N . It can be seen that the standard deviation shows a $\frac{1}{N^2}$ relation and ranges from approximately 0.2 to 0.1 degrees for the perfect image and from 0.7 to 0.2 for the distorted image.

As can be seen, the standard deviation is plotted against $\frac{1}{N^2}$, demonstrating an inverse quadratic relation between the accuracy of our method and the resolution of the image. The linear fits have a coefficient of determination (R^2) of 0.87 and 0.96 for the lower and upper data set, respectively. As anticipated in section 2.6.2, this figure provides an estimate of the parameter space that yields the same cost function and hence showing the theoretical maximum accuracy for a given resolution N .

3.3 Performance

The computational performance of our method is primarily dependent the solving mode. Using the *causal* mode, the NMM is only initiated once using an educated guess based on, for instance, the orientation of the previous frame of a movie. In the *blank* mode, a multitude of initial conditions are evaluated to cover the entire parameter space (ρ) and thus every possible orientation. Since the blank mode is mostly only used once per movie, we only describe the performance of the causal mode.

The parallel scaling study is performed on the Lisa system ². The set of synthetic projections are solved on 1 to 16 threads (processors) and the computation time is recorded. The results are plotted in figure 3.8 for various resolutions.

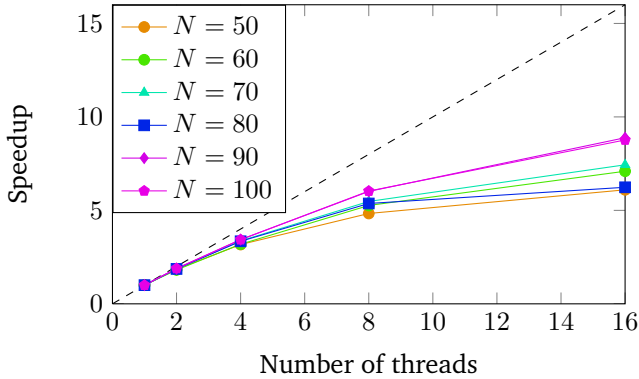


Figure 3.8: Strong scaling of our method, showing the relation between the computation time and number of threads. The dotted line represents perfect strong scaling, where doubling the number of threads yields a doubling of the performance. It can be seen that scaling can be improved by increasing N , which simultaneously increases the accuracy.

It can be seen that this approach scales better for higher resolutions. This can be attributed to the degree of parallelization, as only the computational steps that can be performed in parallel actually speed up. Nevertheless, it was found that with a single thread on an Intel Core 2 Duo 2.53 GHz processor, the method computes approximately ten frames per second when using a resolution of $N = 50$.

²A computer cluster owned by the SURFsara organization.

Chapter 4

Concluding remarks & recommendations

4.1 Conclusions

In part I of this thesis, we have introduced a new method for determining the absolute orientation of a spherical object in three-dimensional space. The theoretical accuracy of the method shows a $\frac{1}{N^2}$ scaling law, where the standard deviation of error for an ideal-case image of 50 by 50 pixels is approximately 0.2 degrees in the Euler angle convention. The addition of pepper & salt noise with a signal-to-noise ratio of 2 reduces the accuracy for the same image size to a standard deviation of 0.7 degrees. Although with significantly decreased accuracy over the ideal case, it shows that the method is still robust under very non-ideal circumstances.

In addition, the method was applied to experiments performed in the Twente Water Tunnel facility to confirm its performance. Physical spheres were painted using various methods, and it was shown that 3-dimensional selective laser sintered (SLS) printed stencils and a paintbrush apparatus yield the best results. Experiments were performed using these spheres which verified that the experimental error is only dependent on the quality

and resolution of the images, and it was shown that for an image size of 50 by 50 pixels, the standard deviation of error is approximately 1.2 degrees. When cropping to a resolution of 80 by 80 pixels, the standard deviation of error is reduced to 0.7 degrees. Although the experimental error is considerably higher than the numerical error, it shows sub-degree accuracy is possible in a practical setting.

Furthermore, it was found that neither blank or causal method required any form of post-processing. This means that the orientation of the previous frame of a (movie) sequence was sufficient to determine that of the current frame. However, this is limited by the difference in orientation between two frames. This limit was not encountered in any of the experiments performed for this paper, and hence a detailed study was not done.

The computational performance of our method is of the order of tens of frames per second using a contemporary standard laptop. In addition, implementation is straightforward as the only preparation is painting the pattern using a stencil.

In conclusion, it is proven that that the method introduced in this thesis offers a fast, accurate and robust way to obtain the absolute orientation of a spherical object.

4.2 Recommendations

Although the method introduced in this thesis outperforms existing algorithms in efficiency and ease of implementation, improvements can be made specifically in the *blank* mode. In most cases, the blank mode is only used once per recording. However, it covers the solution space (ρ) redundantly and chooses the global minimum from 208 initial conditions (26 axes at 8 angles). The pattern is designed to guide the algorithm towards the global minimum, however no study was performed to determine the ideal balance between the pattern, the number of initial simplices and the corresponding initial simplex sizes. However, performance gains are likely when this balance is optimized. Effectively, optimization would reduce the number of initial simplices in the blank method, as well as reduce the

number of iterations in the causal method and hence improving overall performance.

Also, the pre-processing steps are less than optimal. Currently, a Hough transform circle-detection is used to crop the recordings around the sphere and some image enhancements are performed before presenting the images to the algorithm. It would be beneficial to include the pre-processing steps into the main program, and preferably allow multiple-sphere tracking in three dimensions such that all translational as well as rotational degrees of freedom are resolved. Furthermore, our method can be extended to work for ellipsoids and other geometric shapes.

Part II

Rayleigh-Bénard convection

Chapter 5

Introduction

5.1 Natural convection

Natural convection is fluid flow induced by buoyant forces, commonly as a result of temperature differences. These contributions result in mass and heat transfer within a fluid. In a fluid, convection of both mass and heat is possible through diffusion (Brownian motion) and advection (mass or heat is transported by large-scale motion of the fluid). Convection of heat through diffusion alone is called conduction.

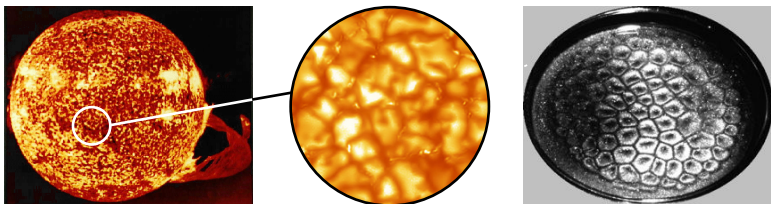


Figure 5.1: Convection examples. The left image shows our sun, with a close-up of the convection patterns in the center image. Note the visual correspondence between the solar surface patterns and the image on the right, which is a pan cooking a fluid. This example shows the vast range of scales of convection, and demonstrates why dimensionless parameters are useful to describe the dynamics of convection.

As the name implies, natural convection has many natural occurrences. For example the motion of the Earth's mantle is considered convection as the hot core drives plumes of magma towards the crust. This process is one of the driving forces of plate tectonics, the process that has formed the shape of the Earth's and other planets' surface. Similar convection patterns are observed in astrophysics, where it is the main mode of energy transport in the sun and other stars for a certain range of radii called the convection zone. An interesting feature of convection is its vast range of scales. Figure 5.1 shows our sun, and a close up of its surface. As comparison, a photograph is shown of a cooking pan heating some viscous fluid. It can be noticed that, although the scales are many orders of magnitude apart, the structures look similar.

5.2 The Boussinesq approximation

In the general case, the behavior of a fluid can be described by the equations of mass, momentum and energy conservation, most importantly the continuity equation and Navier-Stokes equation. That is, the fluids motion is governed by the equations:

$$\frac{\partial \rho}{\partial t} + \nabla \cdot (\rho \mathbf{u}) = 0 \quad (5.1)$$

$$\rho \frac{D\mathbf{u}}{Dt} = -\nabla p + \mu \nabla^2 \mathbf{u} + \mathbf{F}. \quad (5.2)$$

$$\frac{DT}{Dt} = \kappa \nabla^2 T + Q \quad (5.3)$$

Here, the term \mathbf{F} represents any body forces that act upon the fluid, such as gravity. The term Q contains any volumetric heating or cooling.

In buoyancy-driven flow, the body force \mathbf{F} consists of gravitational effects on density variations and thus:

$$\mathbf{F} = \rho \mathbf{g} = (\rho_0 + \Delta \rho) \mathbf{g}. \quad (5.4)$$

The Oberbeck-Boussinesq approximation assumes that variations of all fluid properties are independent of time, temperature and pressure, except the mass density ρ which is assumed linearly dependent on the temperature in the buoyancy term [18]:

$$\Delta\rho = -\alpha\rho_0(T - T_{\text{ref}}), \quad (5.5)$$

where α is the coefficient of expansion of the fluid. We assume no internal heating or cooling and hence, rewriting the Boussinesq approximation in Einstein notation, we obtain

$$\frac{\partial u_i}{\partial x_i} = 0 \quad (5.6)$$

$$\frac{\partial u_i}{\partial t} + u_j \frac{\partial u_i}{\partial x_j} = -\frac{1}{\rho_0} \frac{\partial p}{\partial x_i} + \nu \frac{\partial^2 u_i}{\partial x_j^2} + \alpha g (T - T_{\text{ref}}) \delta_{iz} \quad (5.7)$$

$$\frac{\partial T}{\partial t} + u_j \frac{\partial T}{\partial x_j} = \kappa \frac{\partial^2 T}{\partial x_j^2}. \quad (5.8)$$

The non-dimensionalized equations can be found in appendix B. The resulting dimensionless parameters are the Rayleigh number Ra and the Prandtl number Pr :

$$Ra = \frac{g\alpha\Delta H^3}{\nu\kappa} \quad (5.9)$$

$$Pr = \frac{\nu}{\kappa} \quad (5.10)$$

Here, g is the gravitational constant, α the thermal expansion coefficient, Δ the temperature difference between the top and bottom plate, H is typical length scale, ν the kinematic viscosity and κ the thermal diffusivity of the fluid.

The Rayleigh number can be viewed as the ratio of buoyant forcing of fluid parcels over the viscous drag and thermal diffusion of that fluid parcel. For large Rayleigh number, the flow is strongly driven (i.e. the temperature

difference is high) and the flow is generally more turbulent whereas for low Rayleigh number, the viscosity and/or thermal diffusion dominate the inertial forces and turbulence is suppressed.

The Prandtl number is a fluid property that describes the ratio between the rate at which the fluid diffuses momentum versus heat. If the Prandtl number is high, the fluid tends to attenuate motion strongly by viscous damping and is a relatively bad heat conductor and vice versa.

In addition to Ra and Pr , the geometry of the system determines the convection dynamics. A common model of natural convection is Rayleigh-Bénard (RB) convection and within the scope of this thesis we assume RB convection inside a cuboid geometry as governed by the Boussinesq approximation, although we point out where this approximation loses its validity. The geometry is captured by the non-dimensional aspect ratio's Γ_1 and Γ_2 of the cell which is elaborated in section 5.3.

In response to the input parameters, the transport of heat and momentum can be summarized in two quantities called the Nusselt number Nu and the Reynolds number Re , given by

$$Nu = \frac{\langle u_z T \rangle_{A,t} - \kappa \frac{\partial \langle T \rangle_{A,t}}{\partial z}}{\kappa \Delta T H^{-1}} \quad (5.11)$$

$$Re = \frac{UH}{\nu} \quad (5.12)$$

Here, the Nusselt number can be understood as dimensionless heat transfer between the top and bottom plate. A Nusselt number of 1 corresponds to the case where there is no fluid motion (advection) and only conduction, e.g. heat transfer in a solid. The Reynolds number is defined by the ratio of inertial over viscous forces and provides an indication of the level of kinetic energy within the flow.

The $\langle \cdot \rangle_{A,t}$ denotes an average over a plane at fixed z and time. Note that an additional averaging over the volume reduces Nu to

$$Nu = \frac{\langle u_z T \rangle_{V,t}}{\kappa \Delta T H^{-1}} + 1 \quad (5.13)$$

In addition, the Nusselt number can be computed from the viscous and thermal dissipation rates, given by

$$\epsilon(\mathbf{x}, t) = \frac{\nu}{2} \sum_{i,j} \left(\frac{\partial u_i}{\partial x_j} + \frac{\partial u_j}{\partial x_i} \right)^2 \quad (5.14)$$

$$\epsilon_T(\mathbf{x}, t) = \kappa \sum_i \left(\frac{\partial T}{\partial x_i} \right)^2 \quad (5.15)$$

using the exact relations that can be derived from the Boussinesq approximation. The exact relations are given by [19]

$$\langle \epsilon \rangle = \frac{\nu^3}{H^4} (Nu - 1) Ra Pr^{-2} \quad (5.16)$$

$$\langle \epsilon_T \rangle = \kappa \frac{\Delta T^2}{H^2} Nu \quad (5.17)$$

where $\langle \cdot \rangle$ denotes a statistical ensemble average.

The Reynolds number is computed using a velocity dimension U , typical lengthscale H (the height of the cell) and the kinematic viscosity ν . When using non-dimensional velocities, as is the case in simulation, the velocities are scaled using the free-fall velocity $u_f = \sqrt{g\alpha\Delta TH}$. It can be derived that a convenient Reynolds number can then be defined as

$$Re = \mathbf{u}_{rms} \cdot \sqrt{\frac{Ra}{Pr}} \quad (5.18)$$

Where \mathbf{u}_{rms} is the root-mean-square velocity in non-dimensional units of each direction x , y and z .

5.3 Rayleigh-Bénard convection

Rayleigh-Bénard convection is a model scenario of natural convection that occurs in a two- or three-dimensional container. We refer to this container as a cell which is heated from below and cooled from above.

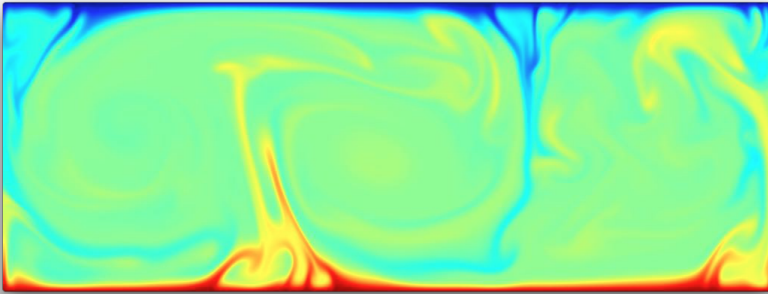


Figure 5.2: Snapshot example of the temperature field for a 2D simulation of a Rayleigh-Bénard cell for $Ra = 10^8$, $Pr = 4.3$ and $\Gamma = 3$. Plumes of hot (red) and cold (blue) fluid are rising and falling due to buoyant forces.

The extent of the cell may be finite or infinite, and various boundary conditions may be imposed. Within this thesis, we define a finite cell of size $H \times W \times L$ and impose no-slip conditions on all faces. In addition, the bottom and top plate are kept at constant temperature and the sidewalls are assumed adiabatic. Figure 5.3 shows a schematic view of a Rayleigh-Bénard cell.

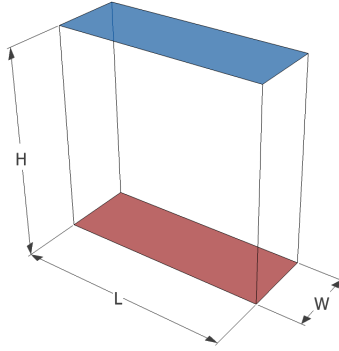


Figure 5.3: Definitions of the thin-cell fluid volume. The cell is non-dimensionalized using the aspect ratio's $\Gamma_1 = \frac{L}{H}$ and $\Gamma_2 = \frac{W}{H}$.

Heat is transported from hot bottom plate to the cool top plate by the aggregate motion of the molecules within the fluid between the plates through diffusion and advection, referred to as *convection*. For small temperature differences, a temperature gradient arises within the fluid and heat is transferred by conduction alone. However, critical $Ra_{\text{crit}} = 1708$ (for no-slip boundary conditions), the temperature difference is sufficient to induce instabilities and advection is initiated. Consequently, the Nusselt number increases from $Nu = 1$ to $Nu > 1$.

Figure 5.4 shows two snapshots of the temperature field of a 3-dimensional Rayleigh-Bénard system where $Ra \gg Ra_{\text{crit}}$. The snapshots show translucent isothermal surfaces, showing the dynamics of the flow.

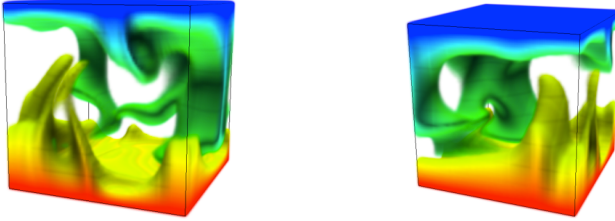


Figure 5.4: Two snapshots of a 3-dimensional Rayleigh-Bénard simulations at different angles and simulation times for illustrative purpose. For this simulation $Ra = 10^7$, $Pr = 4.3$ and $\Gamma_1 = \Gamma_2 = 1$ and no-slip boundary conditions.

The cell is defined as a box of size $H \times W \times L$ which is non-dimensionalized using aspect ratios $\Gamma_1 = \frac{L}{H}$ and $\Gamma_2 = \frac{W}{H}$. A schematic view of the geometry is shown in figure 5.3. We define the directions x , y and z as the direction of width (W), length (L) and height (H) and use these conventions throughout this thesis.

5.4 Experimental methods

Recently, experimental setups designed for high Rayleigh numbers have been studied. For example the *Barrel of Ilmenau*, currently the largest convection cell measuring 7 m by 6.3 m, is used to study highly turbulent convection in air. Similarly, the University of Twente built and maintains a Taylor-Couette (TC) experimental setup. Although geometrically very different, Taylor-Couette and Rayleigh-Bénard systems show profound analogies [20].



Figure 5.5: Barrel of Ilmenau (left), courtesy of Technische Universitaet Ilmenau, Institute of Thermodynamics and Fluid Mechanics and the Twente Turbulent Taylor-Couette system (right), courtesy of the Physics of Fluids Group, University of Twente

For both RB and TC, advanced flow visualization methods such as (3D) PIV/PTV and micro temperature probing are commonly used. However, it is difficult to obtain scalar or vector fields like temperature, pressure or velocity over the entire flow. Therefore, within the Physics of Fluids group at the University of Twente, numerical studies are performed for RB and TC in addition to the TC experimental setups.

For this thesis, a thin-cell Rayleigh-Bénard setup is designed and manufactured, and a relatively novel visualization method called *background-oriented schlieren* is worked out and applied to this setup. Chapter 6 elaborates on this setup.

5.5 Numerical methods

Direct numerical simulations provide a quantitative analysis of the flow by solving the equations of motion down to the smallest physical scales of the flow. In order to fully resolve the flow, the spatial mesh size is equal or

smaller than the smallest physical scale of the flow, i.e. the Kolmogorov length scale.

In contrast to experimental methods, numerical methods provide several benefits regarding data analysis, because flow visualization and statistics are trivial. Additionally, system parameters and boundary conditions can be continuously variable and be specified more precisely. Nevertheless, a major drawback of computer simulation is computational cost. In order to fully resolve the thermal and viscous boundary layers and the smallest scales of the bulk flow, the spatial resolution must be sufficiently high. In addition, the temporal resolution must match the smallest time scales of the flow, while the total simulation time must be sufficiently high to allow for statistical convergence.

To minimize the simulation time, the spatial grid is divided into sections which are individually evaluated by separate processors and subsequently merged to compute the next temporal step. This process called parallel computation has become an active field of research itself, but an elaboration is unfortunately beyond the scope of this thesis.

For this thesis, a novel version of an existing [13] code is developed that allows for direct numerical simulation of 3-dimensional cuboid geometries in Rayleigh-Bénard systems with free- or no-slip boundary conditions. The code is used in chapter 6 to simulate various geometries of the experimental setup. The results are subsequently used to quantify the exact geometry of the setup such that quasi-two-dimensional flow is ensured and schlieren visualization techniques can be applied. In addition, chapter 7 describes a brief numerical study of the heat transport in very small aspect ratio cells using the new code.

Chapter 6

Thin-cell Rayleigh-Bénard convection setup

6.1 Introduction

In the field of fluid physics, Rayleigh-Bénard is widely studied and emphasis is given to understanding the underlying physics by forming theoretical models and scaling laws of turbulent convection. These models and scaling laws are derived from mathematical theory, experiments or numerical studies. In recent years, advances in High-Performance Computing (HPC) have allowed extracting vast amounts of data that would be difficult or impossible to obtain from laboratory experiments. In fact, numerical simulations are used in chapters 6 and 7. Nevertheless, physical experiments provide insight into real-world behavior such as the influence of perturbations, material imperfections and heat loss which are very hard to model. Also, experiments can achieve higher Ra . Therefore, having a physical setup may complement numerical simulations by offering a way of validation and relation to the real world. In addition, an appealing feature of the setup itself is that its phenomena are perpetual; once initiated, there is a constant supply of complex and interesting flow dynamics merely by heating and

cooling. This provides a wonderful showcase of the dynamics of convection inside a confined container.

6.2 Experimental setup

6.2.1 Design

An experimental setup is custom designed and built for the purpose of visualization and data gathering of a quasi-two-dimensional Rayleigh-Bénard system. The setup must be sufficiently flexible to allow studying of a sufficiently large parameter space and be suitable for a multitude of visualization techniques. Also, the heating and cooling elements must employ closed-loop control systems to impose the fixed temperature boundary conditions for the bottom and top plate.

For practical reasons, the experiment must be manageable and transportable by one person, and hence the largest dimension may not exceed approximately 0.5 m. Another important design feature are the cell's size and aspect ratio's. Optical flow visualization techniques like shadowgraph and schlieren are limited to (quasi)-two-dimensional flows¹ and hence the flow must be confined to two dimensions, i.e. $\Gamma_2 \ll \Gamma_1$. The value of Γ_1 describes the aspect ratio of the cross-section, akin to the aspect ratio Γ of a true 2-dimensional systems and determines largely the flow state of the system [15].

An interesting feature of Rayleigh-Bénard systems is the interaction between the large scale circulation and thermal plumes that arise from the boundary layers. Thermal plumes are generally sheared off by the large scale circulation, and rise and fall in-between two rolls. It is therefore decided to design the system for the double/triple roll state, which corresponds to $\Gamma_1 \approx 3$. This ensures there are plumes rising and falling not only at the side boundaries of the cell, but also in the center.

Example snapshots of two-dimensional simulations are shown in figure 6.1.

¹Schlieren-based techniques may be extended to work in multiple dimensions. See section 6.6

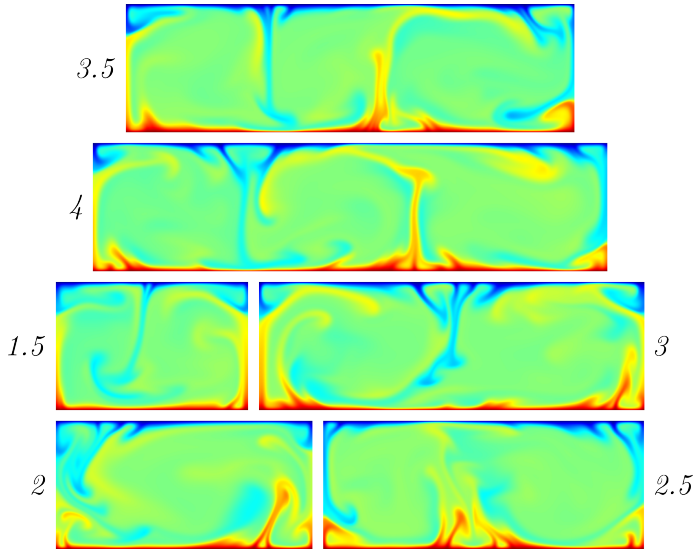


Figure 6.1: Snapshot of the temperature field of 2D simulations for various aspect ratio's for $Pr = 4.3$ and $Ra = 10^7$. The color indicates the temperature, where red corresponds to hot fluid and blue to cold fluid. The aspect ratio Γ is placed alongside the snapshots. For $\Gamma = 3$, a double roll state is observed, while $\Gamma \geq 3.5$ prompts a triple roll state.

For quantification of the forcing parameter Ra , we assume plain demineralized water as working fluid and boundary conditions of 10°C and 50°C at the top and bottom plates. Although the Boussinesq approximation assumes that fluid properties density do not change with temperature (except where it appears as buoyancy term), this is not true for large temperature differences. Therefore, the Boussinesq approximation may be less valid. In addition, the boundary conditions of the sidewalls may not be pure adiabatic.

Near the top and bottom plate, the fluid is generally colder and hotter than average and the properties of the fluid are within a certain range. From [14], we find $0.9 \cdot 10^{-4} \leq \alpha \leq 4.5 \cdot 10^{-4}$, $0.548 \cdot 10^{-3} \leq \nu \leq 1.307 \cdot 10^{-6}$ and $1.38 \cdot 10^{-7} \leq \kappa \leq 1.58 \cdot 10^{-7}$. Therefore, the control parameters are expected to be in the range of

$$10^8 \leq Ra \leq 10^9 \tag{6.1}$$

$$3.5 \leq Pr \leq 9.5 \tag{6.2}$$

The dimensionalization of the physical setup is governed mostly by practical considerations like size and safety. For example, the use of water as working fluid limits the temperature range and fixes certain fluid parameters like the Prandtl number. Also, a brief numerical study of Γ_2 is done to verify that the flow is confined in one dimension, but does not inhibit flow in the other two dimensions. The setup is simulated for $Ra = 10^6$ and $Ra = 10^8$. The Reynolds numbers of the x , y and z directions are computed using eq. (5.18), The time averaged Reynolds number in the direction of narrowing (the x -direction) is divided by that of the y - and z -direction.

The results are shown in figure 6.2.

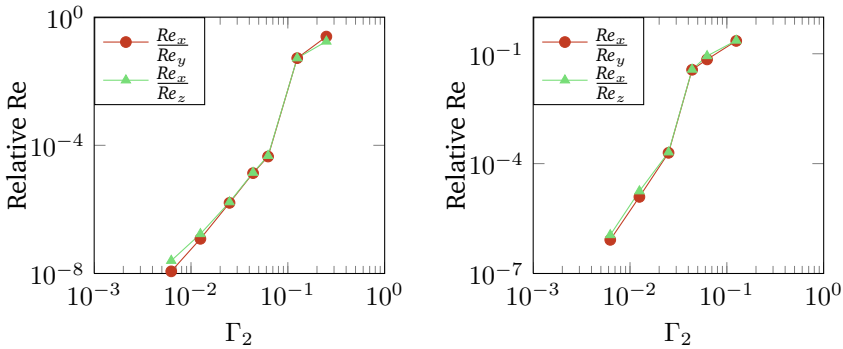


Figure 6.2: Simulation results of relative Re as a function of the narrow aspect ratio Γ_2 for $Pr = 5$, $\Gamma_1 = 3$, $Ra = 10^6$ (left) and $Ra = 10^8$ (right).

It can be seen that the root-mean-square Reynolds number in the direction of narrowing is approximately one order of magnitude smaller than both the other horizontal and vertical direction if $\Gamma < 10^{-1}$. For narrower cells, the relative Reynolds number in the direction of narrowing monotonically decreases down to 10^{-6} for $\Gamma < 10^{-2}$. Therefore, we consider the flow as quasi-two-dimensional for aspect ratio's smaller than 0.1.

The experimental setup is designed in SolidWorks taking into consideration the design parameters as described. The design process consists mainly of solving practical issues like sealing and mounting methods. A rendering of the final setup is shown in figure 6.3.

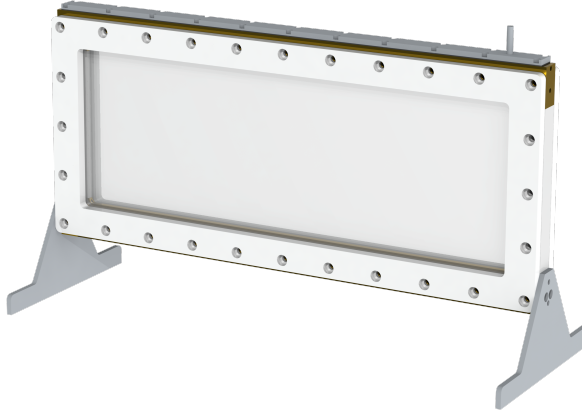


Figure 6.3: Rendering of the setup assembly, consisting of the two transparent plates, top and bottom plate and support structure.

The setup consists of two transparent acrylic glass plates, two plastic (POM) side inlays and a brass top and bottom plate that encapsulate the working fluid. The total volume of encapsulated fluid is 460 mm long, 160 mm high and 5 mm wide. In dimensionless units, this means that $\Gamma_1 = 2.88$ and $\Gamma_2 = 0.031$. From figure 6.2, it can be seen that for an aspect ratio $3.1 \cdot 10^{-2}$, the Reynolds number in the direction of confinement is several orders of magnitude lower than in the other directions and hence we consider the flow quasi-two-dimensional. Using the heating and cooling elements, a temperature difference of approximately 50 degrees Celcius can be realized. In this case, the top plate is kept at 10 degrees Celcius and the bottom plate at 50 degrees Celcius.

The top and bottom plate both consist of single piece of machined brass to ensure heat conduction from the heating or cooling elements to the working fluid. The bottom plate contains holes that encapsulate electric heating elements, and a temperature probe is inserted in any of these voids.

Figure 6.5 shows a cut-through section of the bottom part of the setup, visualizing the heater voids.

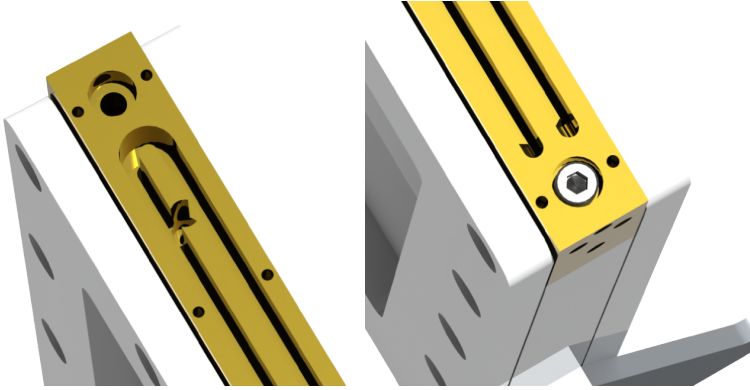


Figure 6.4: Close-up rendering of the U-shaped cooling channel of the top plate at the bend (left) and at the input and output connections (right). Note the number of holes required for the cooling liquid and assembly screws.

The top plate is liquid-cooled using a U-shaped channel that is milled into the plate itself, as is shown in figure 6.4. The cooling liquid is demineralized water that is pumped through the channel, and kept at constant temperature by a cooling unit.

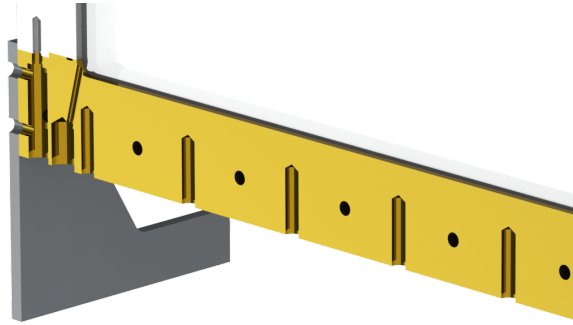


Figure 6.5: Close-up section plane rendering of the electric heating elements. The channel for filling the setup can be seen on the far left of the image.

When demineralized water is used as working fluid and the temperature difference is set to 40°C , the dimensionless forcing parameter Ra and the Prandtl number can be computed. Using equation (5.9) and (5.10) and using the fluid parameters at an average temperature of 30°C , we find

$$Ra = \frac{9.81 \cdot 3.0 \cdot 10^{-4} \cdot 40 \cdot 0.16^3}{0.799 \cdot 10^{-6} \cdot 1.46 \cdot 10^{-7}} \approx 4.1 \cdot 10^9 \quad (6.3)$$

$$Pr = \frac{0.799 \cdot 10^{-6}}{1.46 \cdot 10^{-7}} \approx 5.3 \quad (6.4)$$

6.3 Visualization methods

6.3.1 Theory

Shadowgraphy and schlieren methods are types of flow visualization that make use of density differences induced by temperature variations inside a medium. For transparent media like gases, density differences are not necessarily visible by eye. However, the density (ρ) of a medium is related

to the refractive index (n) through the Lorenz-Lorentz equation, given by

$$\frac{n^2 - 1}{(n^2 + 2)} = K_{LL} \quad (6.5)$$

Where K_{LL} is a function that relates the density to the refractive index. This relation is quite complex, and commonly empirical relations are used. However, it will be shown later in this section, we require the temperature derivative of the refractive index to resolve the temperature from the refractive index. Within the scope of this thesis, we assume that the derivative is constant within our temperature range, i.e. $\frac{dn}{dT} = \text{constant}$.

Traversing light beams will be refracted following the inhomogeneities of the medium, thereby casting shadows where temperature gradients are present as is exploited in shadowgraphy. For example, the thermal plumes of an (invisible) flame, often seen in ethanol fires in bright daylight, will cast clear shadows on surrounding surfaces.

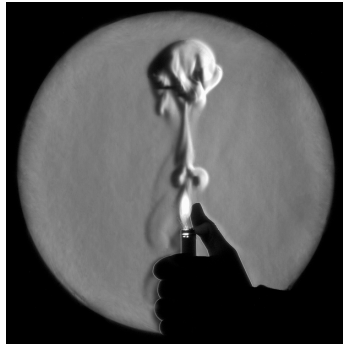


Figure 6.6: In this example, a lighter is lit and the rising plumes of hot air are visualized using shadowgraphy. Image courtesy of Flickr user RachaelDere.

Within the scope of this thesis, we limit flow visualization to qualitative visualization of the temperature field, i.e. a non-dimensionally scaled temperature field. To resolve the temperature field, we derive the relation between the temperature and angle of refraction. Figure 6.7 shows schematically the a ray of light refracting through a medium.

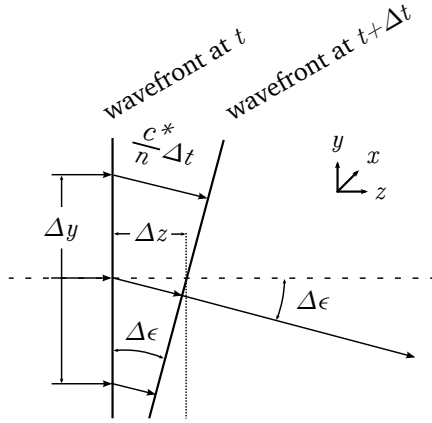


Figure 6.7: Refraction

From figure 6.7, it can be derived that

$$\Delta \epsilon = \frac{\Delta z}{\Delta y} = \frac{(c_y - c_{y+\Delta y}) \Delta t}{\Delta y} \quad (6.6)$$

Given that the local speed of light c_y is given by $\frac{c^*}{n_y}$, we can substitute the index of refraction in the right hand side, yielding

$$c^* \left(\frac{1}{n_y} - \frac{1}{n_{y+\Delta y}} \right) \frac{\Delta t}{\Delta y} = -c^* \Delta \left(\frac{1}{n} \right) \frac{\Delta t}{\Delta y} \quad (6.7)$$

Substituting the distance $c^* \Delta t$ by $n \Delta z$ then gives

$$\Delta \epsilon = -n \Delta \left(\frac{1}{n} \right) \frac{\Delta z}{\Delta y} \quad (6.8)$$

We now substitute the Δ with its infinitesimal counterpart d , which yields

$$d\epsilon = -n d \left(\frac{1}{n} \right) \frac{dn}{dy} dz \quad (6.9)$$

Which can be simplified slightly by merging the index of refraction differential, and noting that the light rays can be refracted in both the x and y direction, we find

$$d\epsilon_y = \frac{1}{n} \frac{\partial n}{\partial y} dz \quad (6.10)$$

The last step is to integrate this over the length of the medium L . Here, we also substitute n_0 , which denotes the index of refraction of the undisturbed fluid. The result is the angle of deflection ϵ as a function of the refractive index gradient

$$\epsilon_y = \frac{L}{n_0} \frac{\partial n}{\partial y} \quad (6.11)$$

The temperature is a function of the index of refraction, i.e. $T = T(n)$. Therefore, the chain rule must be applied and we find

$$\epsilon_y = \frac{L}{n_0} \frac{\partial n}{\partial T} \frac{\partial T}{\partial y} \quad (6.12)$$

The angular deflection ϵ can be related to the virtual displacement of a speckled pattern and from the displacement field, the temperature field can be derived. This is elaborated in section 6.3.3 on background-oriented schlieren.

6.3.2 Shadowgraph imaging

Shadowgraphy is the technique that employs the refractive phenomenon and has applications in science and engineering. It is used in the aerospace industry to visualize high-speed (compressible) flow around aircraft and missiles, as well as the glass industry, where it provides a simple method to visualize non-uniformities in the material.

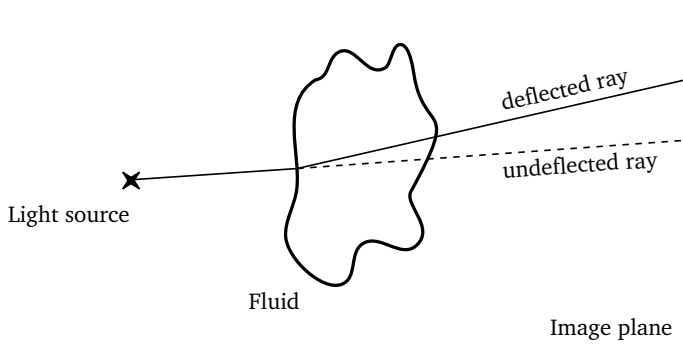


Figure 6.8: Schematic illustration of a shadowgraphy setup. The light rays from the light source traverse the fluid medium and are thereby refracted, causing regions of high and low intensity light at the image plane.

In a shadowgram, the resulting image that shadowgraphy generates, the differences in light intensity I are related to the refractive index field of the medium. Although it is possible to derive the density field and hence the temperature field from a shadowgram, the background-oriented schlieren method is better suited for recovering the said temperature field as is explained in section 6.3.3.

We employ shadowgraphy for demonstrative flow visualization purposes. The goal is to provide a simple accessible tabletop experiment that allows exposition of the dynamics of a Rayleigh-Bénard system using shadowgraph flow visualization.

In addition, the setup must allow for qualitative studying of thin-cell Rayleigh-Bénard flow. Therefore, the setup is constructed such that both shadowgraphy and flow visualization using background-oriented schlieren can be applied. The latter is elaborated in section 6.3.3.

6.3.3 Background-oriented schlieren

General concept

Similar to shadowgraphy, background-oriented schlieren or BOS employs density variations to recover the temperature field of a test section. However, the implementation is quite different and allows a straightforward quantitative reconstruction of the temperature field. It is a relatively novel [17] method of flow visualization that simplifies conventional schlieren visualization considerably by eliminating the need for precision optical components.

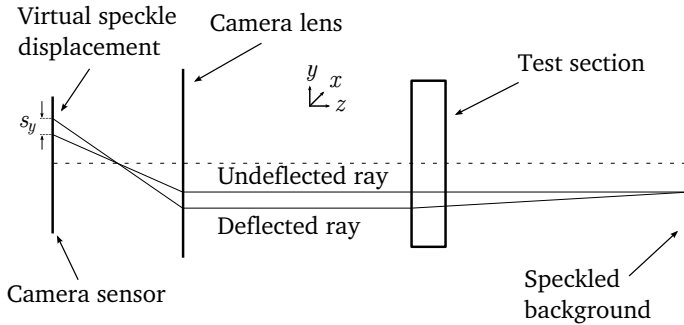


Figure 6.9: Illustration of background-oriented schlieren setup. The light rays originating from a speckle are refracted by variations in the index of refraction of the test section, causing a virtual displacement of that speckle with respect to the undistorted (reference) pattern as recorded by the camera sensor.

Figure shows a schematic illustration of the BOS setup. It consists of an illuminated background screen, a test section, camera and a computer to store and process the recordings. Although conventional schlieren is operated preferably under low light conditions, BOS is not sensitive to such noise. In fact, BOS is based on the virtual displacement of the background image and works with any number of light sources. The pattern on the background screen must provide sufficient contrast and be matched with the resolution of the camera. White noise, consisting of uniformly (random) distributed black pixels on a white background, is well suited for this purpose. We use the term *speckles* to refer to this pattern.

Akin to shadowgraph, traversing light is refracted through the medium. If there were no variations in the index of refraction of the test section, the camera simply records the speckle pattern. However, when temperature gradients inside the test section are present, light rays are bent slightly, which distorts the perception of the speckle pattern as seen from the camera's perspective. This distortion is manifested as a virtual displacement of the individual speckles, and the extent of displacement is proportional to the index of refraction and thus to the temperature. By resolving the speckle displacements relative to a steady calibration pattern, one can resolve the temperature field of that time instance.

The speckle displacements are related to the deflection angle by the geometry of the setup, and therefore the temperature can be resolved. Since we are only interested in the qualitative temperature field, we assume that the displacement is proportionally related to the angle of deflection, i.e. $\epsilon \sim s$. Therefore, we find the following relation between the temperature and displacement

$$s_y = \lambda \frac{\partial T}{\partial y} \quad (6.13)$$

where λ is a proportionality constant that contains the relations between the refractive index, density and temperature and the geometric parameters.

Measurements start by creating a reference recording snapshot of the background with the test section at rest, i.e. no temperature difference is present. Next, the cooler and heater are engaged and the camera starts recording. Each frame of the recording is compared to the reference snapshot to compute the displacement of that time instance. The next section describes the process of analysis and how the temperature field is recovered.

Analysis

Succeeding the measurement, the recorded frames are processed to recover the temperature field. This process consists of computing the displacement of the speckle pattern to obtain the deflection of a light ray caused by variations in the index of refraction.

The displacement is computed using a cross-correlation, a method commonly used in particle image velocimetry (PIV). It is based on the correlation between two images as a function of spatial variations. The image is divided into several subsections called interrogation windows. The spatial variation for which the cross-correlation is maximized, corresponds to the approximate shift of each interrogation window.

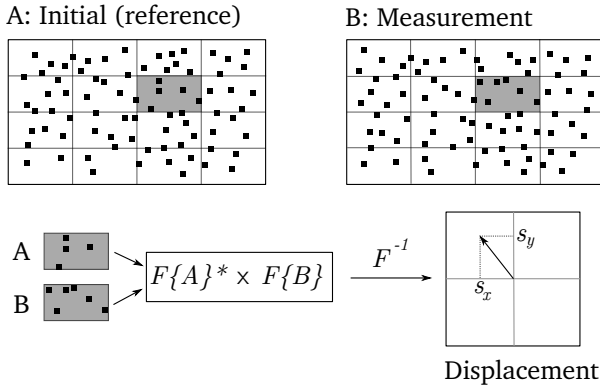


Figure 6.10: Illustration of the computation of speckle displacement using a Fourier transform (denoted by $F\{\cdot\}$) to compute the correlation.

A common performance enhancement is to compute correlation in Fourier space. A cross correlation, defined as

$$(f \star g)(\tau) = \int_{-\infty}^{\infty} f^*(t)g(t + \tau)dt \tag{6.14}$$

also satisfies

$$\mathcal{F}\{f \star g\} = (\mathcal{F}\{f\})^* \cdot \mathcal{F}\{g\} \tag{6.15}$$

where \mathcal{F} denotes the Fourier transform, and the asterisk the complex conjugate. Using fast Fourier transforms, the cross-correlation can be computed very efficiently compared to the regular spatial method.

Next, the displacement field is solved by integrating eq. (6.13). In two dimensions, this means finding the potential function T of a gradient field s , i.e. to solve

$$\nabla T = \lambda s \quad (6.16)$$

Which can be solved by numerical integration of the displacement field s or by transforming the problem into a Poisson problem, i.e. (omitting the proportionality constant)

$$\nabla \cdot (\nabla T) = \nabla \cdot (s) \rightarrow \nabla^2 T = \nabla \cdot s \quad (6.17)$$

Which allows the use of Poisson solvers for which very efficient methods exist.

6.4 Results

6.4.1 Experimental setup

An overview photograph of the experimental setup is shown in figure 6.11. As can be seen from the image, the electric heater elements are inserted into the setup, and the wires are guided towards a central unit. At the top of the setup, the cooling channel is visible, and two tubes for in- and outflow of cooling water are connected. These tubes are connected to a central cooling unit which contains 5 L of temperature-controlled water as cooling buffer. The tubes on the lower right and upper left of the setup are used for filling and emptying the setup with the working fluid.

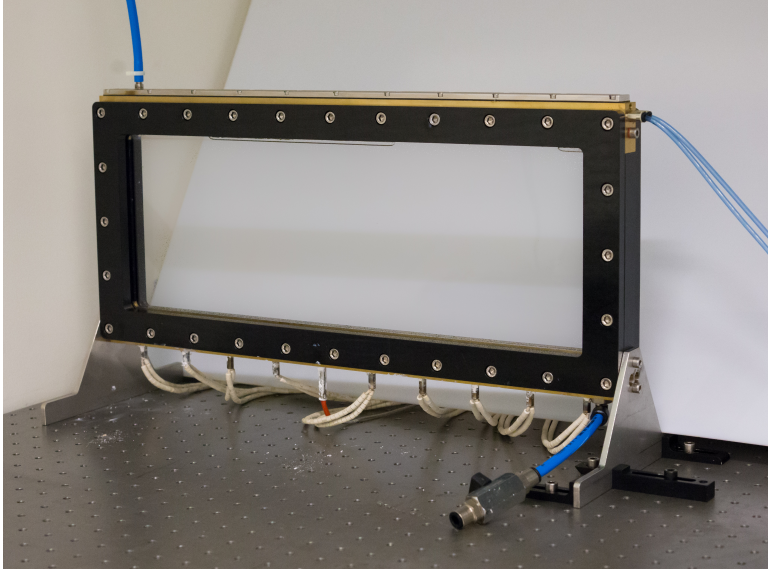


Figure 6.11: Overview photograph of the setup. The bottom plate contains 9 heating elements and a temperature probe in the center. The tube on the bottom right is used for filling the setup, and the top right tubes are cooling tubes. The tube on the left top acts to ensure atmospheric pressure inside the setup.

In figure 6.12, close-ups of the heating elements and cooling channel are shown. In the left picture, the probe slightly deviating in size is the temperature probe, which is inserted into the center hole. The right image shows additional holes which are used for reverse-mounting of the triangular-shaped steel supports. Although it was not used for this thesis, the setup may be reversed, placing the heating elements on top and the cooling element at the bottom.

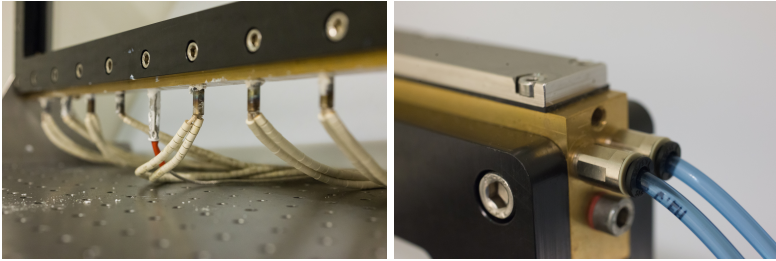


Figure 6.12: Close-up photographs of the electric heating elements (left) and the input and output cooling channels of the top plate (right).

The setup as presented in this section is used for experiments within this thesis. It is a flexible setup, allowing for a large range of parameters including various working fluids to be studied.

6.4.2 Shadowgraphy visualization

In January of 2014, the working setup was displayed at the Physics@FOM congress in Veldhoven. Due to material availability, we used a simple projector as light source and a several sheets of matte A3 paper as screen while the setup was placed onto a table-top. A photograph of the setup is shown in figure 6.13a.

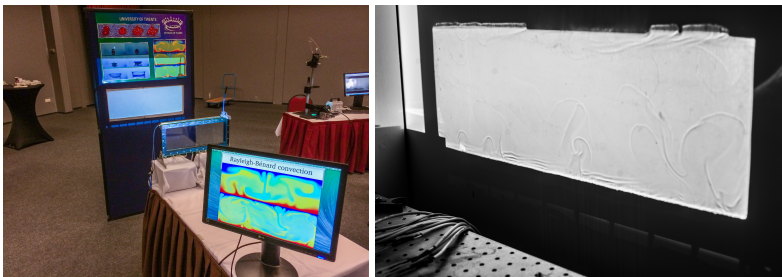


Figure 6.13: Photographs of the setup at the Physics@FOM congress (left) and a shadowgram created by the setup (right).

In figure 6.13b, a close-up photograph of the shadowgram is shown. Unfortunately, it is difficult for a camera to capture the perception as viewed by naked eye. To improve visibility of the thermal structures of the flow, we contrast-adjusted a photograph of the shadowgram which is shown in figure 6.14.



Figure 6.14: Shadowgram as created by the setup. It is difficult to capture the perception as viewed by the naked eye on paper, though this contrast-adjusted image shows good resemblance with the actual shadowgram.

Over the course of several days, the setup was able to gain the attention of both the scientific and general public and proved to be a great introduction to explaining the thermally-driven motion of Rayleigh-Bénard.

6.4.3 Background-oriented schlieren

As stated in 6.3.3, a speckled pattern is generally used as reference background, as the displacements can easily be resolved using PIV methods. Several speckled patterns are tested, and it was found that a salt & pepper pattern with a 30:70 ratio of black and white pixels is well suited as background. However, BOS is a robust technique, and variations in this ratio will not affect the results much.

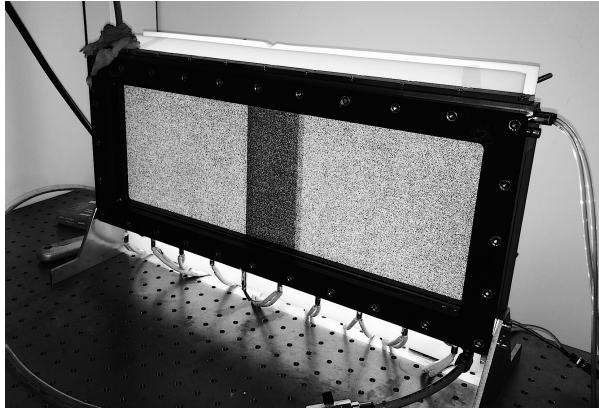


Figure 6.15: Photograph of the setup with the speckled background

Preferably, the entire flow field is recorded simultaneously. However, the camera's sensor resolution and lens' focal distance limit the viewable region of the background to an area of approximately 17×13 cm, which is captured as an image of 1392×1040 pixels. Although calibration is not required since we are interested in qualitative results, it is important that the smallest features of the flow can be resolved by the camera. Based on the results of the shadowgraphy method, it was estimated that the resolution is sufficient to resolve the structures of the flow. Since the resolution of the camera is approximately 0.13 mm/pixel, the speckle size is determined to be least 0.2 mm to ensure the camera can resolve individual speckles. However, no quantitative study was performed for this thesis.

Using the method as described in section 6.3.3, footage of the background is recorded and the displacements are calculated. From these displacements, a relative temperature field is derived by solving the gradient equation (6.16). Example results are shown in figure 6.16. These results were obtained with demineralized water as working fluid, the lower plate set to 60°C and the upper plate set to 10°C .

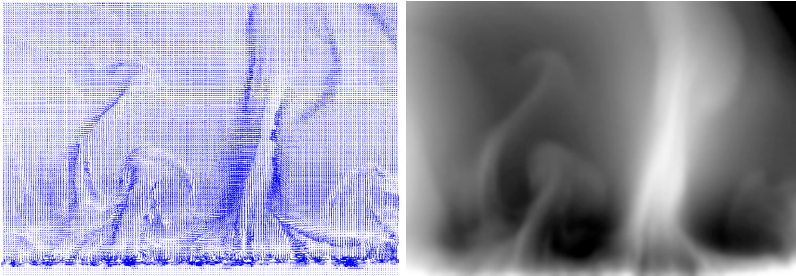


Figure 6.16: The displacement field (left) as computed by PIV and the corresponding normalized temperature as resolved using eq. (6.16) (right). Dark regions correspond to lower temperatures and light regions to hot regions.

It can be seen from figure 6.16 that the temperature field is and that a quantitative result is obtained. By comparison, two snapshots of the same parameters in simulation are shown in figure 6.17. A box is overlaid to the image to illustrate the size of the viewable area from the experiments relative to the complete cell.

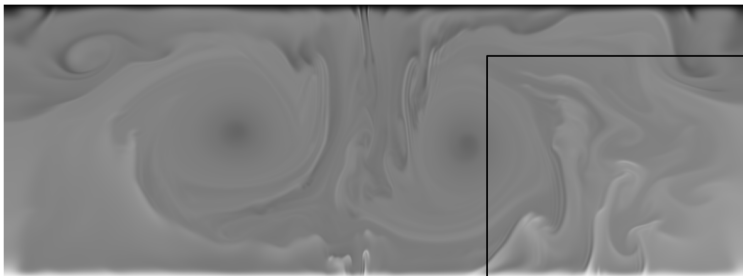


Figure 6.17: Snapshot of the temperature field. For comparison, the same colormap as in figure 6.16 is used. It can be seen that the simulation visually corresponds to the experimental results.

It is clear that the structures of the flow show visually resemble the simulation snapshots, demonstrating a qualitative correspondence between simulation and experiments. From these experiments, statistics on the temperature field such as plume hotspots and scales may be obtained.

Due to time and material restrictions, data collection and analysis is beyond the scope of this thesis. However, as shown in this section, the BOS method provides a reliable way of recovering the temperature field of a Rayleigh-Bénard cell. Recommendations on continuation of research using the experimental setup can be found in section 6.6.

6.5 Derivation of velocity quantities

6.5.1 Hypothesis

Using the background-oriented schlieren technique, a relative temperature field can be obtained. Although the temperature field provides great conceptual insight in the behavior of the flow and thermal plumes therein, the dynamics of the flow are described by the velocity field. The most common method of deriving the velocity field of some flow is to use tracer particles that follow the fluids streamlines. Advanced PIV algorithms can then recover the actual velocity field in great detail. A drawback of this type of flow visualization is that it is invasive; one has to add particles to the fluid and match the density of these particles with the surrounding fluid.

In practice, it sometimes seems that one can deduce the velocity field from the temperature field only by looking at it, specifically in the regions where there is a strong temperature gradient. We hypothesize that the velocity field can be derived from the temperature field alone, assuming only incompressibility and given boundary conditions. In this paragraph, we derive the mathematics of this hypothesis and prove that, unfortunately, this is impossible.

Suppose a temperature field $T(x, y)$. We use incompressibility (eq. (5.6)):

$$\nabla \cdot \mathbf{u} = 0, \tag{6.18}$$

and by the definition of the stream function

$$\psi = \int_A^P u_x dy - v dx \tag{6.19}$$

we can relate the velocity components to the stream function as

$$u = + \frac{\partial \psi}{\partial y} \quad (6.20)$$

$$v = - \frac{\partial \psi}{\partial x} \quad (6.21)$$

As stated in chapter 5, a Rayleigh-Bénard cell must satisfy the convection-diffusion equation (eq. (5.8)), given by

$$\frac{\partial T}{\partial t} = \kappa \nabla^2 T - \mathbf{u} \cdot \nabla T \quad (6.22)$$

Written out in differential form:

$$\frac{\partial T}{\partial t} - \kappa \left(\frac{\partial^2 T}{\partial x^2} + \frac{\partial^2 T}{\partial y^2} \right) + u \frac{\partial T}{\partial x} + v \frac{\partial T}{\partial y} = 0 \quad (6.23)$$

Substituting eq. (6.20) and (6.21) we obtain

$$\frac{\partial T}{\partial t} - \kappa \left(\frac{\partial^2 T}{\partial x^2} + \frac{\partial^2 T}{\partial y^2} \right) + \frac{\partial \psi}{\partial y} \frac{\partial T}{\partial x} - \frac{\partial \psi}{\partial x} \frac{\partial T}{\partial y} = 0 \quad (6.24)$$

We assumed that the temperature is derived from the background-oriented schlieren method and hence this equation can be rewritten to

$$\alpha \frac{\partial \psi}{\partial x} + \beta \frac{\partial \psi}{\partial y} = \gamma \quad (6.25)$$

where $\alpha = \frac{\partial \psi}{\partial y}$, $\beta = -\frac{\partial \psi}{\partial x}$ and $\gamma = \kappa \left(\frac{\partial^2 T}{\partial x^2} + \frac{\partial^2 T}{\partial y^2} \right) - \frac{\partial T}{\partial t}$. This is a linear ordinary differential equation that can be rewritten to solve $Ax = b$ for x and can generally be solved as a system of linear equations or using iterative methods like Gauss-Seidel relaxation. From the gradient of the solved quantity ψ , the vertical and horizontal velocity components are easily derived.

Although equation (6.25) can indeed be solved, it is mathematically impossible to *uniquely* derive u and v from T , which is proven in section 6.5.2.

6.5.2 Proof

The proof for this is based on the fact that any velocity field \mathbf{v} that is solenoidal, perpendicular to T and satisfies the boundary conditions can be added to \mathbf{u} such that the conservation laws still hold.

More formally, the question is whether there exists some (non-trivial) $\mathbf{v} \in \mathbb{R}^2$ such that $\mathbf{w} = \mathbf{u} + \mathbf{v}$ satisfies the convection-diffusion and continuity equation and corresponding boundary conditions. Consequently, if there exists such \mathbf{v} , then \mathbf{u} cannot be uniquely retrieved because only \mathbf{w} can be recovered.

Restrictions on \mathbf{v}

Starting with the generalized proof in 3 dimensions, we consider the convection-diffusion equation (5.8). The temperature is assumed to be obtained from some experiment and is thus a known quantity in space and time. We can then simplify eq. (5.8) to

$$\mathbf{u} \cdot \nabla T = L(\mathbf{x}), \quad (6.26)$$

where $L = -\partial_t T + \kappa \nabla^2 T$ and $\mathbf{x} = (x, y, z)$. Now consider a solution $\mathbf{w} = \mathbf{u} + \mathbf{v}$, substitution then gives

$$(\mathbf{u} + \mathbf{v}) \cdot \nabla T = L \quad (6.27)$$

Working out the brackets, this yields

$$\mathbf{u} \cdot \nabla T + \mathbf{v} \cdot \nabla T = L \quad (6.28)$$

It is clear that when $\mathbf{v} \perp \nabla T$, this equation is equal to (6.26) which infers the first condition:

$$\boxed{\mathbf{v} \cdot \nabla T = 0} \quad (6.29)$$

Second, the substitution must satisfy the continuity equation

$$\nabla \cdot \mathbf{u} = 0 \quad (6.30)$$

and after substitution we find

$$\nabla \cdot (\mathbf{u} + \mathbf{v}) = 0 \quad (6.31)$$

Again, working out the brackets:

$$\nabla \cdot \mathbf{u} + \nabla \cdot \mathbf{v} = 0 \quad (6.32)$$

It is clear that when \mathbf{v} is divergence-free, the equation is equal to the original incompressibility equation, and hence the second condition is derived:

$$\boxed{\nabla \cdot \mathbf{v} = 0} \quad (6.33)$$

Third, \mathbf{v} must satisfy the boundary conditions. For Dirichlet boundary conditions (no-slip boundary conditions) on a domain Ω , i.e. $\mathbf{u}(\mathbf{x}) = \mathbf{u}_0(\mathbf{x}) \forall \mathbf{x} \in \partial\Omega$, the substitution must also hold. Therefore, it must hold that

$$\mathbf{w}(\mathbf{x}) = (\mathbf{u}(\mathbf{x}) + \mathbf{v}(\mathbf{x})) = \mathbf{u}_0(\mathbf{x}) \forall \mathbf{x} \in \partial\Omega \quad (6.34)$$

which imposes $\mathbf{v}(\mathbf{x}) = 0 \forall \mathbf{x} \in \partial\Omega$ as boundary condition.

Similarly, if Neumann boundary conditions are imposed on the domain Ω , i.e.

$$\frac{\partial \mathbf{u}}{\partial \mathbf{n}}(\mathbf{x}) = \mathbf{q}(\mathbf{x}) \forall \mathbf{x} \in \partial\Omega \quad (6.35)$$

where \mathbf{n} is the vector normal to the boundary $\partial\Omega$ and \mathbf{q} is some function at the boundary.

It can be derived that it must hold for \mathbf{v} that

$$\frac{\partial \mathbf{v}}{\partial \mathbf{n}} = 0 \quad (6.36)$$

Generalized existence proof in three dimensions

To prove that there exists a \mathbf{v} , we provide an example. Consider the vector field

$$\mathbf{v} = \nabla \times (h\nabla T) \quad (6.37)$$

where $h = h(x, y, z)$ is an arbitrary scalar function. For the first restriction, substitution into (6.29) gives

$$(\nabla \times (h\nabla T)) \cdot \nabla T = 0 \quad (6.38)$$

Using the vector identity $\nabla \times (\psi \mathbf{A}) = \psi \nabla \times \mathbf{A} + \mathbf{A} \times \nabla \psi$ and substituting ∇T for \mathbf{A} , we find

$$(h\nabla \times \nabla T + \nabla h \times \nabla T) \cdot \nabla T = 0 \quad (6.39)$$

The above relation is true $\forall h$, because the cross product of a gradient is always zero and because $(\mathbf{A} \times \mathbf{B}) \cdot \mathbf{B} = 0 \forall \mathbf{A}$. Hence, eq. (6.29) is satisfied.

For the second restriction, substitution into (6.33) gives

$$\nabla \cdot (\nabla \times (h\nabla T)) = 0 \quad (6.40)$$

Which is also satisfied $\forall h$ because the divergence of the curl of a vector field is zero by definition.

For Dirichlet boundary conditions, demanding $h(\mathbf{x}) = 0 \forall \mathbf{x} \in \partial\Omega$ satisfies the boundary condition restriction and does not restrict h in the rest of the domain. Similarly, Neumann boundary conditions do not restrict h in rest of the domain. Therefore, all restrictions are satisfied, proving that \mathbf{u} can *not* uniquely be recovered from the temperature field.

Proof in two dimensions

The hypothesis is based on the assumption of a stream function, which can only be defined in two dimensions. To prove that there exists a similar \mathbf{v} in two dimensions, we again provide an example. Also, we consider ∇ as two-dimensional operator and use both ∂_x and $\frac{\partial}{\partial x}$ interchangeably as partial derivative operators.

Consider the vector field

$$\mathbf{v} = (f\partial_y T, -f\partial_x T)^\top \quad (6.41)$$

where f is an arbitrary function of T , i.e. $f = f(T)$. Substituting (6.41) into (6.29) gives

$$(f\partial_y T, -f\partial_x T)^\top \cdot \nabla T = 0 \quad (6.42)$$

Writing out the components then gives

$$(f\partial_y T \partial_x T) + (-f\partial_x T \partial_y T) = 0 \quad (6.43)$$

which is true $\forall f$ because multiplication is commutative and thus (6.41) satisfies the first condition.

Substituting (6.41) into the incompressibility condition (6.33) gives

$$\nabla \cdot (f\partial_y T, -f\partial_x T)^\top = 0 \quad (6.44)$$

Working out the operator yields

$$\partial_x (f\partial_y T) + \partial_y (-f\partial_x T) = 0 \quad (6.45)$$

Which can be written out using the product rule and chain rule for f . For the x -derivative, this yields

$$\partial_x (f \partial_y T) = \frac{\partial f}{\partial T} \frac{\partial T}{\partial x} \frac{\partial T}{\partial y} + f \frac{\partial^2 T}{\partial x \partial y} \quad (6.46)$$

And similarly for the y -derivative:

$$\partial_y (-f \partial_x T) = -\frac{\partial f}{\partial T} \frac{\partial T}{\partial y} \frac{\partial T}{\partial x} - f \frac{\partial^2 T}{\partial y \partial x} \quad (6.47)$$

It can be seen that adding (6.46) and (6.47) equals zero $\forall f$ and thus equation (6.45) is true $\forall f$. Therefore, the second condition is satisfied.

Similar to the three-dimensional case, the boundary conditions do not impose additional restrictions on \mathbf{v} and hence it suffices to demand $f(\mathbf{x}) = 0 \forall \mathbf{x} \in \partial\Omega$ for Dirichlet boundary conditions.

6.6 Conclusions & recommendations

In this chapter, we have shown the successful design and build of an experimental Rayleigh-Bénard setup. The setup allows for various visualization techniques of which shadowgraphy and background-oriented schlieren are applied. Shadowgraphy visualization is used for demonstrative purposes at the Physics@FOM congress, at which the setup received interest from both the scientific and general public. The background-oriented schlieren method was successfully applied to the experimental Rayleigh-Bénard setup built for this thesis and a relative temperature field is obtained using the BOS method. It was hypothesized that BOS would also allow the recovery of the velocity field, but as proven in section 6.5, this is mathematically impossible.

It was shown that background-oriented schlieren is a robust method to determine the relative temperature field in two dimensions. Similar to discrete tomography applications in medical imaging, a method may be developed that allows resolving the temperature field in three dimensions. Such a setup would consist of a transparent fluid container, a speckled screen on one side and an array of camera's opposite to the screen. The camera array must be aligned such that the speckled screen is viewed

through the fluid container from various angles. From the multitude of computed displacement fields, the temperature field may then be reconstructed. This technique would allow non-invasive measurement of the relative temperature field in three dimensions, and it is recommended to study the feasibility of this method.

Chapter 7

Spatially confined thermal convection cells

7.1 Introduction

In many domestic and industrial applications, the ability to enhance or decrease the heat transport is of crucial importance. Examples range from small-scale electronics to heat management of real estate. Using geometrical confinement to manage heat transport is well-known in the field of fluid physics [15], and the goal in general is to optimize heat transport by changing the cell's aspect ratios. As sidewalls enforce no-slip conditions which cause the viscous boundary layers to increase relative to the cell's size, it is intuitively expected that narrowing even further will only increase drag force, thereby decrease advection and thus reduce heat transport. Recently [16], however, confinement induced heat transport enhancement for very narrow cells (aspect ratios of order 10^{-1}).

In this short chapter, we show the effect of spatial confinement of thermal convection for a wider range of aspect ratios. We use direct numerical simulations (DNS) to study the heat transport in cells of aspect ratios from 10^{-3} to 1.

7.2 Background & method

The geometry of a Rayleigh-Bénard cell has a significant effect on its flow behavior. It was recently shown [15] that the aspect ratio in two-dimensional systems has a significant influence on the dynamics as well as the heat transfer of that system. The dynamics of a system can be categorized in certain modes called *flow states*. For example, the dynamics of a two-dimensional system with aspect ratio $\Gamma \approx 1$ can form a single roll state (SRS) where there is one cell-sized large scale circulation. If the aspect ratio is increased, the number of rolls can increase, as is shown schematically in figure 7.1.

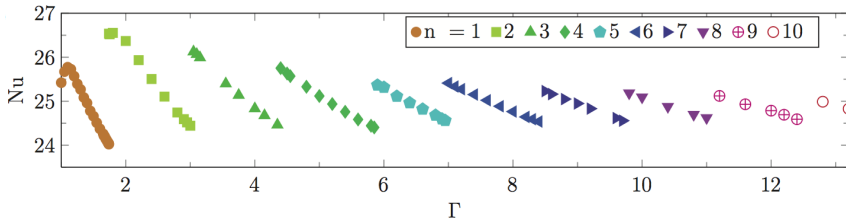


Figure 7.1: Nusselt number as a function of Γ for $Ra = 10^8$ and $Pr = 4.3$ for $1 < \Gamma < 12$. It can be seen that the aspect ratio has a significant effect on the dynamics of the system, illustrated by 10 clusters of points that represent the SRS up to the horizontally stacked 10RS. Courtesy of [15].

These flow structures are closely related to the Nusselt number, as the fluids advection dynamics determine how efficient heat is transported from the bottom to the top plate.

Using direct numerical simulation of the Boussinesq equations, we simulate Rayleigh-Bénard cells of various aspect ratio's and at several values of Ra . We choose a non-uniform grid spacing of our simulation mesh such that the boundary layers are sufficiently resolved. In addition, an *a posteriori* analysis is done of each simulation verifying that it is sufficiently resolved by comparing the time-averaged global Nusselt number computed from the volume-integrated kinetic thermal energy dissipation rates to the time-averaged Nusselt number as computed over each horizontal slice.

For analysis, we study the volume-average Nu (eq. (5.13)) and the root-mean-square Re_{rms} averaged over each grid direction x , y and z .

7.3 Results

Several cell sizes for various forcing parameters are simulated. Figure 7.2 shows the normalized Nusselt number as a function of the confinement aspect ratio Γ_2 . The Nusselt numbers are normalized to $Nu = 1$ at $\Gamma_2 = 1$ for each set.

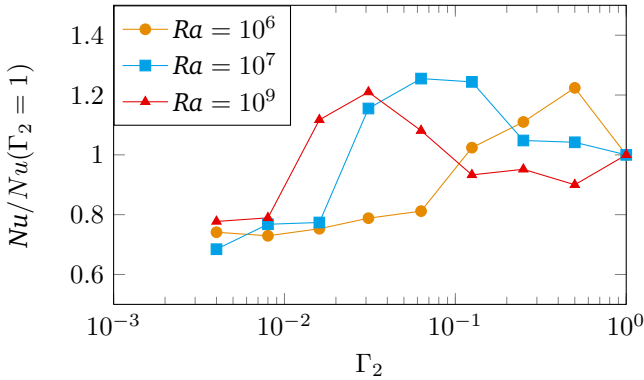


Figure 7.2: Normalized Nu for $Pr = 4.3$, various Ra as a function of Γ_2 . It can be seen that Nu increases for light confinement ($\Gamma_2 < 1$). For moderate confinement, Nu peaks and decreases for strong confinement.

It can be seen that the Nusselt number increases for moderate confinement. The increase is significant, and seems to increase steeper for smaller Ra . When decreasing the aspect ratio even further, however, the increase in Nu peaks and starts to decrease. For $Ra = 10^6$, the peak is around $\Gamma_2 \approx \frac{1}{2}$, and the peak shifts to $\Gamma_2 \approx \frac{1}{32}$ for $Ra = 10^9$. Figure 7.3 shows the peak, denoted by Γ_{opt} , as a function of Ra .

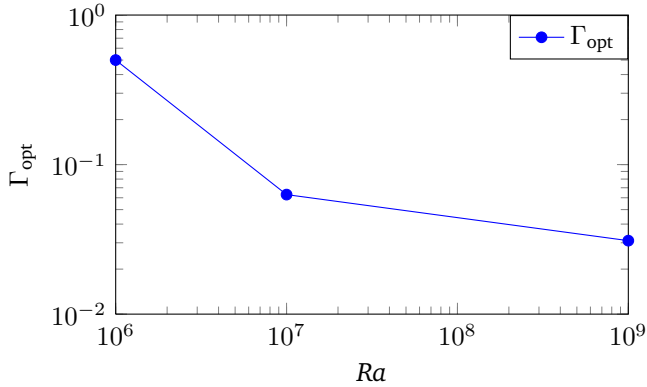


Figure 7.3: Γ_{opt} as a function of Ra . Although there are only three datapoints in this plot, a monotonic inverse trend can be seen. It is expected that Γ_{opt} decreases for increasing Ra due to the smaller thermal boundary layer and thermal plumes.

Although this plot only contains three datapoints, a monotonic inverse relation can clearly be seen. It is expected that this is caused by the decreasing size of the thermal boundary layer and corresponding thermal plumes for higher Ra .

To couple the heat transfer increase to the flow dynamics in the x , y and z directions, the time and volume averaged Reynolds numbers are shown in figure 7.4.

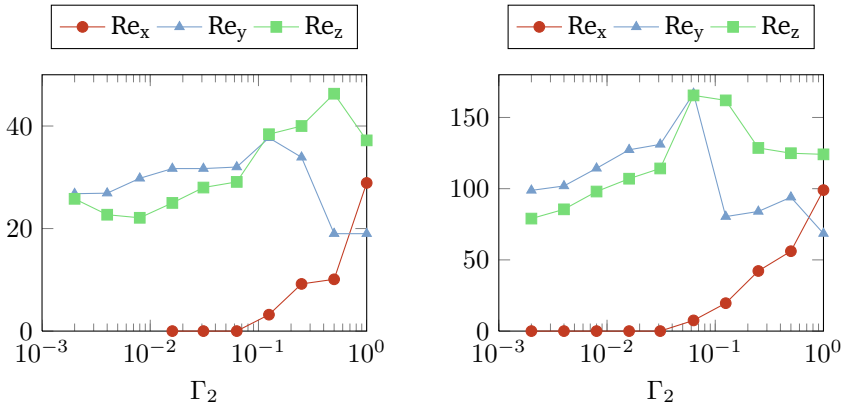


Figure 7.4: Re_{rms} for $Ra = 10^6$ (left) and $Ra = 10^7$. $Pr = 4.3$ for both sets. It can be seen that the geometric confinement restricts the flow in the direction of narrowing, while an increase is observed in perpendicular directions.

It is clear that the geometric confinement restricts flow in the x -direction for $Ra = 10^6$ and $Ra = 10^7$. As the aspect ratio decreases, an initial increase in Nu is observed as shown in 7.2. It can be seen that this is accompanied by a strong increase in Re_y and Re_z .

7.4 Conclusions & recommendations

In this chapter, the heat transport in spatially confined thermal convection cells was studied for $\frac{1}{256} \leq \Gamma_2 \leq 1$ and $Pr = 4.3$. It was shown that for $Ra = 10^6$, 10^7 and 10^9 , Nu increases, peaks and subsequently decreases and that the aspect ratio Γ_{opt} for which Nu is highest, decreases for higher Ra .

This result is rather counter-intuitive as it is expected that spatial confinement would increase viscous drag from the walls and therefore slow down the flow, leading to a decrease of Nu . However, although confinement does increase drag from the sidewalls, for light to moderate confinement this is actually beneficial to heat transport as the large scale circulation (LSC) is damped.

It is generally known that an LSC has a profound effect on the dynamics of the thermal plumes, as they are carried along by the flow. Huang et al. [16] has found that the local temperature profile at the cell center and its PDF change from exponential to Gaussian-like with decreasing Γ and states that this is accompanied by an increasing number of thermal plumes (compared to a lack of plumes for an exponential temperature PDF). The increase in heat transfer may thus be attributed to the damping of the LSC, allowing the thermal plumes to rise upwards through the center of the cell (not being carried around by the LSC) and transfer their heat more efficiently, leading to an increase in Nu . This corresponds to their experimental and numerical results, as shown in figure 7.5 which shows an increase of Nu for light to moderate confinement.

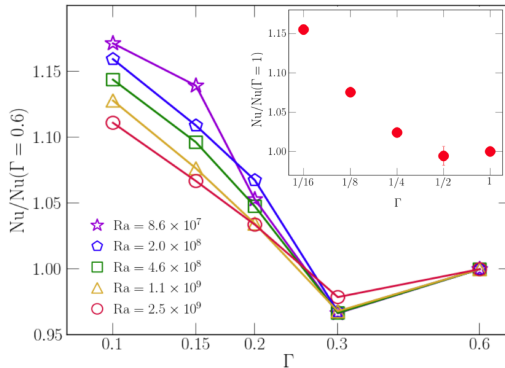


Figure 7.5: Experimentally measured and numerically computed (inlay) normalized Nu as a function of Γ for various Ra and $Pr = 4.3$. It can be seen that Nu increases as Γ decreases. Courtesy of [16].

For strong confinement, however (i.e. $\Gamma \lesssim \frac{1}{2}$ for $Ra = 10^6$, $\Gamma \lesssim \frac{1}{16}$ for $Ra = 10^7$ and $\Gamma \lesssim \frac{1}{32}$ for $Ra = 10^9$), we demonstrated a decrease in Nu as Γ is decreased. It is expected that this may be attributed to the intuitive effect of spatial confinement, where the viscous drag overcomes the buoyancy of the thermal plumes such that the flow is slowed down overall. This hypothesis is supported by the decrease in Re_z and, to lesser extent Re_y .

In conclusion, it is clear that this brief chapter is not sufficient to fully understand the underlying physics of heat transport in spatially confined

thermal convection cells. It is therefore recommended to continue research in this area, for example by increasing the resolution of the parameter space in Γ and Ra . This would allow for determining the exact Γ_{opt} for which heat transport is optimal and provide insight into the flow dynamics at and around this point. The increased parameter space would also allow for a more elaborate $\Gamma_{\text{opt}}(Ra)$ relation. We expect that further study of heat transport optimization by spatial confinement is beneficial for many practical applications. For example passive cooling elements in electronics industry are designed for optimal heat transport by natural convection.

Acknowledgements

First and foremost, I would like to thank my daily supervisor Erwin van der Poel. Working with you has been great throughout my graduation period and it's been a privilege to collaborate with you on physics and mathematics problems. You have a seemingly unlimited capacity of comprehension of various subjects and were always willing to share your knowledge, of which I am very grateful. I wish you the best of luck with your doctorate and beyond, though I am convinced that you will be alright.

Next, I would like to thank Chao Sun and Herman Offerhaus of my supervising committee; I hope that you have enjoyed reading my thesis, and thank you in advance for attending my presentation and grading my work. Also, I am thankful to professor and chairman of the Physics of Fluids group Detlef Lohse for giving me the chance to graduate within his group. I have learned a tremendous amount and have enjoyed the courses that I attended, one of which was the turbulence class which you personally lectured.

I am also indebted to David Goluskin and Charles Doering for their advice and sharing their knowledge regarding the derivation of velocity quantities. You have been very supportive of which I am very grateful.

Furthermore, thank you to the people in the Physics of Fluids group who have been very supportive, specifically Sander Wildeman, Pascal Sleutel, Roeland van der Veen and Sander Huisman for support regarding the experimental setup, Tobias Foertsch for proposing the painting stencil and Vivek Prakash for support with the Twente Water Tunnel and all others that have been supportive. I would also like to thank the technical and secretary staff Gert-Wim Bruggert, Bas Benschop, Martin Bos and Joanita Leferink.

To the students that have been with me in the student room: it's been fantastic. Specifically Maurice Hendrix, Stef Carelsen and Loek Lubbers with whom I have spent numerous productive and not-so-productive days. I wish you the best of luck with your future careers. Also, thanks and good luck to Maarten Kok and Erik Linnartz, with whom I've had innumerable discussions on a wide range of subjects and have been very supportive. Furthermore, Dennis Bakhuis, who I also wish the best of luck with his graduation on Rayleigh-Bénard.

Finally, I would like to thank my parents and family for their continuous support throughout my studies. I greatly appreciate it and could not have done it without you.

Enschede, May 2014

Bibliography

- [1] Burkardt, J. (2008) *Nelder-Mead Minimization Algorithm* (FORTRAN90 version). Retrieved from http://people.sc.fsu.edu/~jburkardt/f_src/asa047/asa047.html
- [2] La Porta, A. et. al. (2001) *Fluid particle accelerations in fully developed turbulence*. Nature (London) 409, pp. 1017-1019.
- [3] Maas, H.G. et. al. (1993) *Particle tracking velocimetry in three-dimensional flows*. Exp. Fluids 15, pp. 133-146.
- [4] Nelder, J.A. and Mead, R (1965) *A simplex method for function minimization*. The Computer Journal 7, pp. 308-313
- [5] Prakash, V. N. et. al. (2012) *How gravity and size affect the acceleration statistics of bubbles in turbulence*. New Journal of Physics 14, 105017.
- [6] Toschi, F. and Bodenschatz, E. (2009) *Lagrangian Properties of Particles in Turbulence*. Annu. Rev. Fluid Mech. 41, pp. 375-404.
- [7] Zimmerman, R. et. al. (2011) *Tracking the dynamics of translation and absolute orientation of a sphere in a turbulent flow*. Rev. Sci. Instr. 82, 033906.
- [8] Zimmerman, R. et al. (2011) *Rotational Intermittency and Turbulence Induced Lift Experienced by Large Particles in a Turbulent Flow*. Phys. Rev. Lett. 106, 154501.
- [9] Ye, J. and Roco, M.C. (1991) *Particle rotation in a Couette flow* Phys. Fluids A 4, No. 2, pp 220-224.

- [10] Frish, M.B. and Webb, W.W. (1981) *Direct measurement of vorticity by optical probe*. J. Fluid. Mech. 107, pp. 173-200.
- [11] Lagarias, J.C. et. al. (1998) *Convergence properties of the Nelder-Mead simplex method in low dimensions*. SIAM J. Optim 9, No. 1, pp. 112-147
- [12] Chillà, F. and Schumacher, J. (2012) *New perspectives in turbulent Rayleigh-Bénard convection* Eur. Phys. J. E 35: 58.
- [13] Verzicco, R. and Orlandi, P. (1995) *A Finite-Difference Scheme for Three-Dimensional Incompressible Flows in Cylindrical Coordinates*. J. Comput. Phys. 123, pp 402-414.
- [14] Kundu, P.K. and Cohen, I.M. (2008) *Fluid Mechanics, Fourth edition*. Burlington, MA: Elsevier Academic Press.
- [15] van der Poel, E.P. et. al. (2012) *Flow states in two-dimensional Rayleigh-Bénard convection as a function of aspect-ratio and Rayleigh number*. Phys. Fluids 24, 085104.
- [16] Huang, S. et. al. (2013) *Confinement induced heat transport enhancement in turbulent thermal convection*. Phys. Rev. Lett 111, 104501.
- [17] Richard, H. and Raffel, M. (2001) *Principle and applications of the background oriented schlieren (BOS) method*. Meas. Sci. Technol. 12, pp. 1576-1585.
- [18] Tritton, D.J. (1988) *Physical Fluid Dynamics*. Oxford, UK: Oxford University Press.
- [19] Shraiman, B.I. and Siggia, E.D. (1990) *Heat transport in high-Rayleigh-number convection*. Phys. Rev. A 42, No. 6, pp. 3650-3653.
- [20] Eckhard, B. et. al. (2006) *What Rayleigh-Bénard, Taylor-Couette and Pipe Flows have in Common*. Nonlinear Phenomena in Complex Systems 9, 109

Appendices

Appendix A

Sphere pattern in FORTRAN syntax

The code below is a modified excerpt of the full code that describes analytical pattern function $F(\theta, \phi)$ in FORTRAN syntax.

```
1      subroutine pattern(theta, phi, s)
2
3      implicit none
4
5      !---- Input and output variables
6      real, intent(in) :: theta, phi
7      integer, intent(out) :: s
8
9      !---- Internal variables
10     real :: y, z
11
12     !---- Internal parameters
13     real, parameter :: bw = 0.353553390593274 ! sqrt(2)/4
14     real, parameter :: pi = 3.141592653589793
15     real, parameter :: pi2 = pi/2
16
17     real, parameter :: num5 = 60.0/180.0*pi
18     real, parameter :: num6 = 90.0/180.0*pi
19     real, parameter :: num7 = 120.0/180.0*pi
20     real, parameter :: num10 = 180.0/180.0*pi
```

```
21     real, parameter :: num11 = 210.0/180.0*pi
22     real, parameter :: num12 = 330.0/180.0*pi
23
24     !---- Limit theta angle
25     theta = mod(mod(theta,2.0*pi)+2.0*pi,2.0*pi)
26
27     !---- Initialize output to zero
28     s = 0
29
30     !---- Region-based pattern function F(theta,phi)
31     if (theta >= pi .and. phi >= pi2) then
32         s = 1
33     elseif (theta <= pi .and. phi <= pi2) then
34         s = 1
35     endif
36
37
38     if ( (phi >= num6) .and. (phi <= num7) .and. (theta >= num12) ) then
39         s = 0
40     endif
41
42     if ( (phi >= num5 .and. phi <= num6) .and. (theta >= num10 .and. theta <=
43         num11) ) then
44         s = 1
45     endif
46
47     y = sin(phi)*sin(theta)
48     z = cos(phi)
49
50     if ( (abs(sin(phi)*cos(theta)) <= (bw + y)) .and. (theta > pi) ) then
51         s = 1
52     endif
53
54     if ( (abs(sin(phi)*cos(theta)) <= (bw - z)) .and. (theta < pi) ) then
55         s = 0
56     endif
57
58     end subroutine pattern
```

Appendix B

Non-dimensionalization of Boussinesq approximation

Suppose Navier-Stokes and convection diffusion equation assuming incompressibility and no sources:

$$\frac{\partial u_i}{\partial t} + u_j \frac{\partial u_i}{\partial x_j} = -\frac{1}{\rho} \frac{\partial p}{\partial x_i} + \nu \frac{\partial^2 u_i}{\partial x_j^2} + g\rho \hat{e}_z \quad (\text{B.1})$$

$$\frac{\partial T}{\partial t} + u_j \frac{\partial T}{\partial x_j} = \kappa \frac{\partial^2 T}{\partial x_j^2} \quad (\text{B.2})$$

The Oberbeck-Boussinesq (OB) approximation then states that ν and κ are not functions of time and ρ is only time-dependent in the buoyancy term. This yields the buoyancy term in NS reduces to $g\beta (T - T_{\text{top}})$ where T_{top} is the temperature of the top plate (and T_{bottom} the bottom plate).

Now using the following non-dimensionalization:

$$u^* = \frac{u}{U_f} \quad (\text{B.3})$$

$$x^* = \frac{x}{L} \quad (\text{B.4})$$

$$t^* = \frac{t}{t_f} \quad (\text{B.5})$$

$$p^* = \frac{p}{\rho U_f^2} \quad (\text{B.6})$$

$$\Theta = \frac{T - T_{\text{top}}}{T_{\text{top}} - T_{\text{bottom}}} \quad (\text{B.7})$$

Here, L is the height of the cell, U_f is called the free-fall velocity and t_f is called the free-fall time. This is obtained by assuming inviscid NS and equating the forcing term ($g\beta\Delta$) to an acceleration. Then $\frac{d^2s}{dt^2} = g\beta\Delta$ which yields a free-fall time $t_f = \sqrt{\frac{L}{g\beta\Delta}}$ and thus free-fall velocity $U_f = \sqrt{g\beta\Delta L}$. The factor $\frac{1}{2}$ is disregarded for clarity and has no effect on the (non-)dimensionalization.

Then substituting everything:

$$\frac{\partial u_i^* U_f}{\partial t^* t_f} + u_j^* U_f \frac{\partial u_i^* U_f}{\partial x_j^* L} = -\frac{1}{\rho} \frac{\partial p^* \rho U_f^2}{\partial x_i^* L} + \nu \frac{\partial^2 u_i^* U_f}{\partial (x_j^*)^2 L^2} + g\beta (T - T_{\text{top}}) \hat{e}_z \quad (\text{B.8})$$

$$\frac{\partial \Theta \Delta + T_{\text{top}}}{\partial t^* t_f} + u_j^* U_f \frac{\partial \Theta \Delta + T_{\text{top}}}{\partial x_j^* L} = \kappa \frac{\partial^2 \Theta \Delta + T_{\text{top}}}{\partial (x_j^*)^2 L^2} \quad (\text{B.9})$$

Navier-Stokes

The first term of NS:

$$\frac{\partial u_i^* U_f}{\partial t^* t_f} = \frac{\partial u_i^* \sqrt{g\beta\Delta}}{\partial t^* \sqrt{\frac{L}{g\beta\Delta}}} = g\beta\Delta \frac{\partial u_i^*}{\partial t^*} \quad (\text{B.10})$$

And the convective term

$$u_j^* U_f \frac{\partial u_i^* U_f}{\partial x_j^* L} = u_j^* \sqrt{g\beta\Delta L} \frac{\partial u_i^* \sqrt{g\beta\Delta L}}{\partial x_j^* L} = g\beta\Delta u_j^* \frac{\partial u_i^*}{\partial x_j^*} \quad (\text{B.11})$$

And the pressure term:

$$\frac{1}{\rho} \frac{\partial p^* \rho U_f^2}{\partial x_i^* L} = \frac{1}{\rho} \frac{\partial p^* \rho (g\beta\Delta L)}{\partial x_i^* L} = g\beta\Delta \frac{\partial p^*}{\partial x_i^*} \quad (\text{B.12})$$

And the diffusive term:

$$\nu \frac{\partial^2 u_i^* U_f}{\partial (x_j^*)^2 L^2} = \nu \frac{\partial^2 u_i^* \sqrt{g\beta\Delta L}}{\partial x_j^* L^2} = \nu \frac{1}{L^2} \sqrt{g\beta\Delta L} \frac{\partial^2 u_i^*}{\partial (x_j^*)^2} \quad (\text{B.13})$$

Dividing every term of NS by $g\beta\Delta$ then yields (dropping the asterixes)

$$\frac{\partial u_i}{\partial t} + u_j \frac{\partial u_i}{\partial x_j} = -\frac{\partial p}{\partial x_i} + \sqrt{\frac{\text{Pr}}{\text{Ra}}} \frac{\partial^2 u_i}{\partial x_j^2} + \Theta \hat{e}_z \quad (\text{B.14})$$

With $\text{Pr} = \frac{\nu}{\kappa}$ and $\text{Ra} = \frac{g\beta\Delta L^3}{\nu\kappa}$.

Convection diffusion temperature

Firstly, the factor T_{top} is constant and drops out, leaving:

$$\frac{\partial \Theta \Delta}{\partial t^* t_f} + u_j^* U_f \frac{\partial \Theta \Delta}{\partial x_j^* L} = \kappa \frac{\partial^2 \Theta \Delta}{\partial (x_j^*)^2 L^2} \quad (\text{B.15})$$

Then the first term:

$$\frac{\partial \Theta \Delta}{\partial t^* t_f} = \Delta \sqrt{\frac{g \beta \Delta}{L}} \frac{\partial \Theta}{\partial t^*} \quad (\text{B.16})$$

And the second term:

$$u_j^* U_f \frac{\partial \Theta \Delta}{\partial x_j^* L} = \sqrt{g \beta \Delta L} \frac{\Delta}{L} u_j^* \frac{\partial \Theta}{\partial x_j^*} \quad (\text{B.17})$$

And the last term right of the equal sign:

$$\kappa \frac{\partial^2 \Theta \Delta}{\partial (x_j^*)^2 L^2} = \kappa \frac{\Delta}{L^2} \frac{\partial^2 \Theta}{\partial (x_j^*)^2} \quad (\text{B.18})$$

Dividing everything by $\sqrt{\frac{g \beta \Delta^3}{L}}$ then yields (dropping the asterixes again):

$$\frac{\partial \Theta}{\partial t} + u_j \frac{\partial \Theta}{\partial x_j} = \sqrt{\frac{1}{\text{RaPr}}} \frac{\partial^2 \Theta}{\partial x_j^2} \quad (\text{B.19})$$